Biologically Inspired Mechanisms for Burrowing in Undersea Substrates

by

Amos Greene Winter, V

B.S.M.E., Tufts University (2003)
M.S.M.E., Massachusetts Institute of Technology (2005)

Submitted to the Department of Mechanical Engineering
in partial fulfillment of the requirements for the degree of

Doctor of Philosophy in Mechanical Engineering

at the

MASSACHUSETTS INSTITUTE OF TECHNOLOGY

February 2011

Author .....
Department of Mechanical Engineering
September 15, 2010

Certified by .....
Anette E. Hosoi
Associate Professor of Mechanical Engineering
Thesis Supervisor

Accepted by .....
David E. Hardt
Chairman, Department Committee on Graduate Theses

Biologically Inspired Mechanisms for Burrowing in Undersea Substrates

by

Amos Greene Winter, V

Submitted to the Department of Mechanical Engineering
on September 15, 2010, in partial fulfillment of the
requirements for the degree of
Doctor of Philosophy in Mechanical Engineering

Abstract

The aim of the research presented in this thesis is to generate compact, lightweight, low-energy, reversible, and dynamic burrowing systems for use in subsea applications such as anchoring, oil recovery, underwater cable installation, mine detonation, and sensor placement. As many organisms have evolved to embed themselves within undersea substrates, unsurprisingly, nature has provided a viable basis for a novel, efficient burrowing technology.

This work centers around understanding the burrowing mechanisms of *Ensis directus*, the Atlantic razor clam, which was discovered to burrow by using motions of its valves to locally fluidize the surrounding substrate. Moving through fluidized, rather than static, soil reduces drag forces to a level within the animal's strength capabilities and results in burrowing energy that scales linearly with depth, rather than depth squared. As *Ensis* contracts its valves, the resulting stress imbalance within the soil creates a failure surface around the clam, within which particles can freely move and fluidize, and outside of which the soil remains static. Theoretical derivations and experimental results demonstrate that the location of the failure surface can be predicted using only two parameters commonly measured in geotechnical surveys: coefficient of lateral earth pressure and friction angle.

To explore the feasibility of transferring localized fluidization burrowing into engineering applications, RoboClam, a robot that burrows using the same mechanisms as *Ensis*, was designed, constructed, and tested. Experimental data show the machine is able to match the animal's linear burrowing energy versus depth relationship and achieve localized fluidization in both granular and cohesive substrates.

Thesis Supervisor: Anette E. Hosoi
Title: Associate Professor of Mechanical Engineering

Acknowledgments

I was fortunate to have a wonderful PhD experience, facilitated by numerous people in and around MIT who impacted me intellectually, academically, and emotionally. Above all others, Prof. Anette "Peko" Hosoi, my advisor, and Dr. Robert Carnes, my project supervisor from Battelle, the primary sponsor of this research, were instrumental in every stage of my personal and professional development during this time of my life. Peko is the most gifted manager of people with whom I have ever interacted and (I am sure her entire research group would agree with this sentiment) the best advisor in the department. Her brilliance lies in her ability to tailor her advising strategy for each student, encouraging freedom and pushing focus when necessary. She inspires through her enthusiasm and, even when giving critical feedback, forces introspection while leaving you feeling confident in your abilities. Furthermore, she is a phenomenal scientist, able to weave insight, intuition, and theory into a clear, coherent articulation of her research. When I am a professor, I know I will regularly ask myself "what would Peko do?" In my book, she is the benchmark of a great advisor.

Rob Carnes is responsible for making my PhD happen. I am forever thankful to him for believing in me after our first meeting and taking it upon himself to find funding for this project. Throughout my entire PhD, he has been an unwavering advocate for my research and for me personally, providing encouragement, freedom, and resources necessary to put my plans into action. Rob has one of the largest intellectual breadths of anyone I know; he continually broadens my life scope through engaging discussions and great book recommendations, and he made significant contributions to my research through his insight and suggestions. Rob is one of the most valued mentors I have had in my life. I look forward to many more years of his guidance and advice.

Prof. Alex Slocum, my PhD co-advisor, was also an enormous presence in my life at MIT. From my first semester as a graduate student, taking his 2.75 Precision Machine Design class, Alex has been an inspiration for me – his passion for engineering

is infectious and I deeply respect his boundless creativity and ability to perform any "back-of-the-envelope" design calculation. Alex and the rest of my thesis committee were a dream team. I appreciated everyones' complementary backgrounds and our meetings were always fun, lively brainstorming sessions. Dr. Jack Germaine brought valuable experience in soil mechanics and perspective of a civil engineer. Prof. Doug Hart is a jack-of-all-trades engineer, with expertise in fluids, particle image velocimetry, and machine design, and had excellent insight on the entire project. And Prof. Chris Rogers from Tufts University continued his unbroken streak, starting from my freshman year at Tufts, as an invaluable mentor in all things scientific, academic, and personal.

Complementary to my thesis committee, a few individuals deserve recognition as part of my "life committee" for their contributions to my personal growth and for shaping my experience at MIT. Prof. Mary Boyce took me under her wing during a difficult semester before I transitioned into a the Hosoi Group. Prof. Dan Frey supported many of my projects related to wheelchair design in developing countries and I look forward to continuing to work with him as a postdoc. Sally Susnowitz, head of MIT's Public Service Center, granted me my first fellowship to study wheelchair technology in developing countries and has supported my projects, and those of many of the students who have worked with me throughout the world, ever since. And Amy Smith, head of MIT's D-Lab program, has been a tremendous friend, mentor, and inspiration during graduate school, helping grow my wheelchair-related programs and shape my desire to include international development as one of the core facets of my career.

Many members of the D-Lab program also made valued contributions to my experience at MIT: Prof. J. Kim Vandiver, Gwyn Jones, Victor Grau Serrat, Jose Gomez-Marquez, Dennis Nagel, Alison Hynd, Laura Sampath, Camilla Shannon, and Kimberly Benard. I am also thankful for being surrounded by so many brilliant and enthusiastic people in both the Hosoi and Precision Engineering Research Groups; thank you for your friendship, stimulating conversations "talking shop," and for creating an intellectually collaborative environment. Outside of the lab, Prof. Wes

Harris, Sandra Harris, Donna Denoncourt, and the New House 3 dorm played a large role in my life during my five-year tenure as a Graduate Resident Tutor.

I am deeply appreciative of all the help I was given by MIT staff during my time in graduate school. In particular, Leslie Regan is an MIT treasure; she helped me navigate some difficult times and I credit her as one of the primary reasons I had such a positive PhD experience. Leslie's colleagues in the ME graduate office, Joan Kravit and Una Sheehan, as well as the following administrators, were a pleasure to work with: Laura Kampas, Debbie Blanchard, Sean Buhmester, Joan Hutchins, Jori Barabino, Mary Ellen Sinkus, Janice McCarthy, Maggie Sullivan, Maureen Lynch, Angela Mickunas, Paula Cogliano, Sandi Lipnoski, and Amy Fitzgerald. I built a lot of hardware during my various projects, which would not have happened without the help of the following workshop coordinators: Mark Bellanger, Tony Caloggero, Ken Stone, Hayami Arakawa, Mike Tarkanian, Dick Fenner, Todd Billings, and Gerry Wentworth. I would also like to thank David Sargent, the Gloucester, MA Shellfish Constable, for training me how to find and catch razor clams.

I could not have accomplished this PhD or pursued my wheelchair projects without the help of many undergraduate researchers. Robin Deits and Dan Dorsch were rockstars on the RoboClam project, making numerous technical contributions and demonstrating resolute commitment, even during 4:00am trips to Gloucester, MA to test the robot. Mario Bollini also deserves special recognition as a brilliant partner in crime during the past four years while making wheelchairs together all over the world and helping advance RoboClam technology. Additionally, it was a pleasure to advise and work with the following senior thesis, MIT Undergraduate Research Opportunities Program (UROP), and MIT Public Service Center students: Tish Scolnik, Harry OHanley, Ben Judge, Amanda Maguire, Caitrin Jones, Chris Becker, Nathan Wang, Lindsay Todman, Nydia Ruleman, Dani Hicks, Danielle DeLatte, Arni Lehto, Xuefeng Chen, Laura Schuhrke, Neeharika Bhartiya, John Walton, Danielle Whited, Katie Ray, Forrest Funnel, Sam Duffley, Sebastian Sovero, Cindy Walker, Joel Sadler, and Kim Harrison. I would also like to thank Melissa Martin Green, head of the UROP program, for providing funding and support for many of these students.

The work in this thesis was financially sponsored by the Battelle Memorial Institute, Bluefin Robotics, and Chevron. Within Battelle, I would like to thank Steve Kelly, Jeffery Wadsworth, Melissa Dixon, Barry McGraw, and Diana Ellis for their support. At Bluefin, special thanks go to David Kelly, Brian Abraham, Lou Quartararo, Chuck Koustas, Jeff Smith, Knut Streitlien, Van Livieratos, Huck Dorn, Thaddeus Stefanov-Wagner, Leo Gurfinkel, David Lewis, Josh Eck, Eddie Huo, Mike Szegedi, James Thomas, Ian Monteith, Richard Wilson, Debra Overland, and Deanna Abraham.

Of course, friends played a large role in my time at MIT. I'd like to thank those with whom I shared great experiences both inside and outside the lab: Nate Landsiedel, Spencer Szczesny, Darius Golda, Kartik Varadarajan, Kevin Lin, John Hart, Hong Ma, Shriram Krishnan, Randy Ewoldt, Tony Yu, Dawn Wendell, Sungyon Lee, Brian Chan, Lisa Burton, and Nadia Cheng. I would also like to thank my wonderful friends from outside MIT who supported me along the way, including: Alex Benjamin, Signe Peterson Flieger, Katie Yacubian, Abby Newcomer, Ben Gallup, Rilda Kissel, Mark Jeunnette, Chuck and Natalie McGraw, Brian Burbank, Katie Nordstrom, and Wheeler Boyd-Boffa. Finally, many thanks go to the friends from around the world that I have made while working on wheelchairs, in particular: Alex Galvez, Joel and Juan Chiti, Hugo and Edgar Andrino, Juanito Buch, Luis Chutan, Fredy Ejcalon, Nazario Quino, Josie Silverman, Abdullah Munish, Fatuma Acan, Peter Mbugua, George and Jose Manongi, Ralf Hotchkiss, Matt McCambridge, Aaron Wheeler, Keoke King, and Marc Krizak.

I could not have completed my degree without my family, quite literally in a biological sense, but more importantly because their emotional support was unwavering throughout my entire time at MIT. I credit my mom, Peet Winter, for my love of engineering; she is very much an engineer in her own right, able to brilliantly form 2D fabric into complex, beautiful wedding dresses. I thank her for an upbringing that fostered creativity through art, music, and tinkering. I also thank my sister Lilly, my mom's partner Gerry Croteau, my aunt and uncle Ann and Bruce Ibarguen, my cousin Keith Ibarguen and his wife Christine, the Klaski family, Dan Rath, and my

grandmothers Mary Groleau and Lillian Winter for creating environments away from MIT for respite and mental recalibration. Finally, the love of my life, Anne Healy, has been a pillar of support and positive encouragement since my freshman year of college. She continually inspires me with her work ethic and dedication, and I credit her with initiating my interest in international development. I look forward to a life together, traveling the world to address pressing social and technological problems.

Contents

Chapter 1

Introduction

The aim of the research presented in this thesis is to generate compact, lightweight, low-energy, reversible, and dynamic subsea burrowing systems. The resulting technology is relavant to applications including anchoring, oil recovery, underwater cable installation, mine detonation, and sensor placement. As many organisms have evolved to embed themselves into undersea substrates, unsurprisingly, nature has provided a viable basis for a novel, efficient burrowing technology. This thesis focuses on *Ensis directus*, the Atlantic razor clam, and transferring the animal's phenomenal burrowing performance into engineering applications. The remainder of this chapter is devoted to describing the background of the project and why *Ensis* was chosen as the basis for a new biomimetic technology. The second chapter presents the discovery of how razor clams locally fluidize the soil surrounding their body to drastically reduce drag and burrowing energy. The third chapter focuses on describing the fluid and soil constitutive behavior at play during localized fluidization. The fourth chapter outlines the creation RoboClam, a robot that burrows using the same mechanisms as *Ensis*, and presents data showing the machine is able to achieve localized fluidization burrowing. Finally, the fifth chapter provides conclusions for the thesis, as well as directions and future work related to research and commercialization of localized fluidization burrowing technology.

1.1 Motivation and applications

There are numerous applications where a compact, lightweight, reversible burrowing system would provide advantages over currently available technology. For example, Bluefin Robotics [1], one of the sponsors of the research presented in this thesis, makes autonomous underwater vehicles (AUVs), such as the one shown in Fig. 1-1A, that navigate the ocean without human control. Applications of AUVs include scientific exploration, national security, and geological surveys. In some circumstances, the robots need to maintain a position, sometimes in a current, and ideally without expending the finite supply of energy in their batteries. Previous design solutions have involved landing the AUV on the ocean bottom and making it negatively buoyant, as to prevent it from being swept away by currents. Such a solution puts the AUV in a precarious position where it could become stuck in mud, entangled in vegetation, or not float to the surface due to failure of its emergency systems.

An alternative would be to station the AUV a safe distance away from the ocean bottom and secure it with a small anchor. A biologically-inspired anchor that can self-burrow into the soil, reposition if necessary, and retract when the AUV needs to relocate would be advantageous. Furthermore, volume and energy are at a premium on an AUV and are best used for mission-critical tasks such as sensing and propulsion. Any AUV anchoring system would have to be compact and require as little energy as possible.

The idea of small, self-inserting and retracting anchors also has significant value in the offshore and oil industries. Figure 1-1B shows a 20 ton drag anchor used to secure oil rigs. The energy required to transport such a device can be estimated as $E = F\delta$, where F is a resistance force due gravity or the hydrodynamic drag on the transporting ship, and δ is distance traveled. Resistance force in either case scales linearly with the anchor's mass; as such, smaller, lighter anchors could provide significant energetic advantages, as well as being easier and safer to handle.

Any existing anchor must be set, or at least retrieved, with human intervention

[1] Bluefin Robotics. 237 Putnam Avenue, Cambridge, MA 02139. http://www.bluefinrobotics.com/

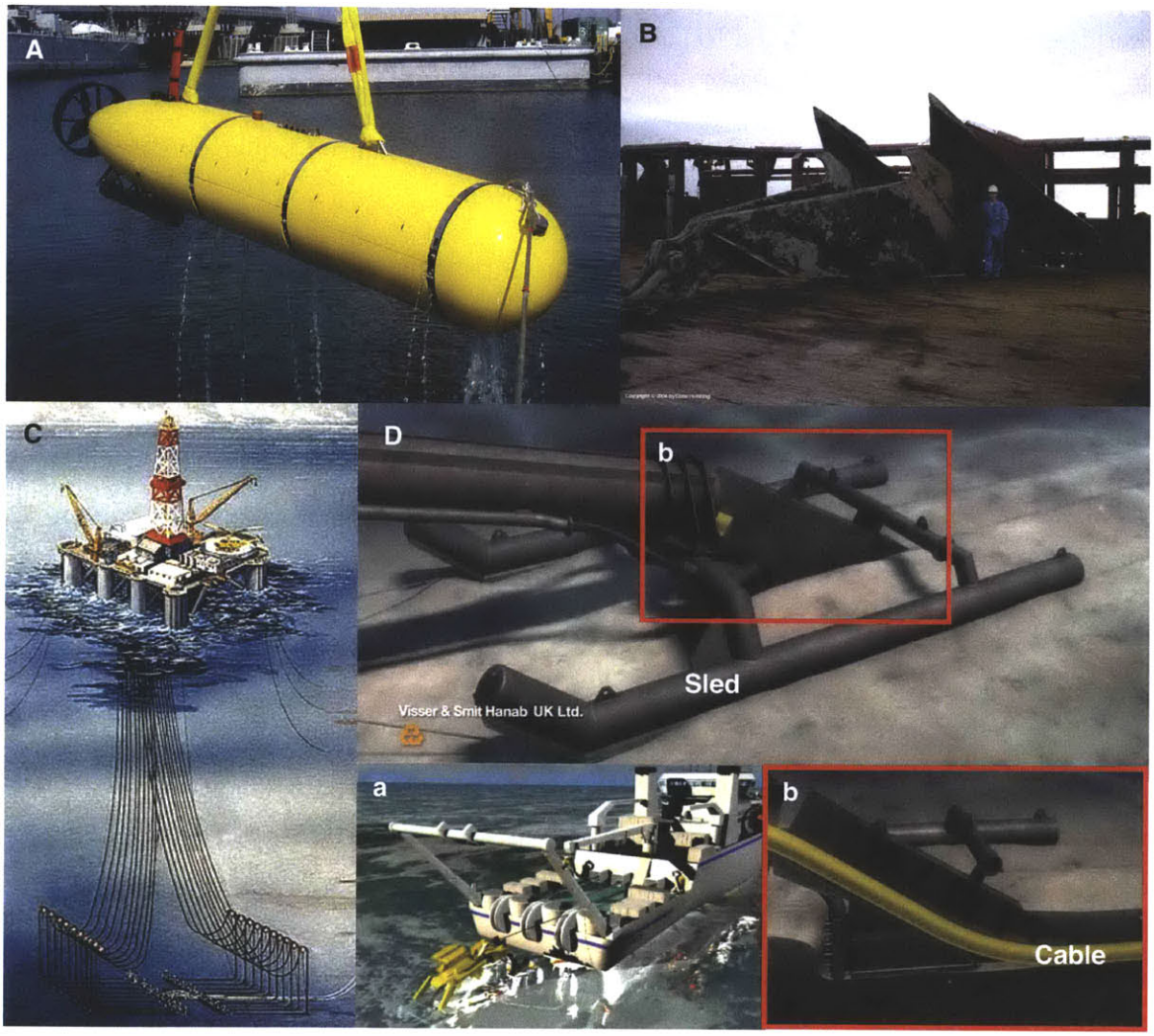

Figure 1-1: Examples of undersea systems that could benefit from localized fluidization burrowing technology. A) Autonomous underwater vehicles [5]. B) Large, offshore anchors [31]. C) Ultra-deepwater oil recovery equipment [57]. D) Underwater cable trenching and installation sleds [81]. Inset a) shows a cable laying sled being deployed from a tow ship [72]. Inset b) shows how the sled cuts a furrow into the soil and lays the cable.

[29, 50], either directly or with a remotely operated vehicle (ROV). This can be tricky in applications such as ultra-deepwater oil drilling, where ocean depths as great as 4,000m [10] complicate the installation of moorings and oil recovery equipment, such as those shown in Figure 1-1C. A system that enables this equipment to be lowered and then autonomously affixed to the ocean bottom, as well as autonomously released for retrieval, would be highly valuable. Such a system would be applicable to a wide range of other subsea systems, including placement of ocean sensors and neutralization of underwater mines.

A final example of an application for the burrowing technology presented in this thesis is subsea cable and pipe installation. Cables and pipes are commonly embedded into the ocean bottom via a sled pulled behind a ship [54, 56], as shown in Fig. 1-1D. This system of installation can only be used in water depths greater than 15 to 20m, as the draft of the ship prevents entering shallower regions. As a result, cables in depths from 20m to the shore must be manually buried by divers - a process that is tremendously expensive and yields approximately 25m of installation per day [56]. An alternative method of installation, using the technology presented in this thesis, would be to create a device that affixes to the cable and moves axially, burying the cable as it travels. Such a device could be used in any water depth and automate cable installation in shallow and littoral zones.

1.2 Biomimetics and burrowing technologies

Biomimetics is an area of research and engineering where new technologies are created by mimicking systems found in nature [96]. This field has gained significant popularity and exposure in recent years with well known technologies such as those shown in Fig. 1-2.

In regards to biomimetics and burrowing, there are many examples of animals that live in particulate substrates that have adapted unique locomotion schemes. The sandfish lizard (*S. scincus*) undulates in the manner of a fish in order to effectively swim through sand [47]. Clam worms (*N. virens*) have been observed to use crack

Figure 1-2: Examples of biomimetic inspirations and technology. A) Velcro® was invented by Georges de Mestral after he saw burs similar to the one pictured [34] stuck to his cloths and dog after a hike [80]. B) The Big Dog robot was designed to navigate rough terrain like a four-legged animal [6]. C) Mercedes Benz made this car aerodynamic by modeling its form after a fish [62].

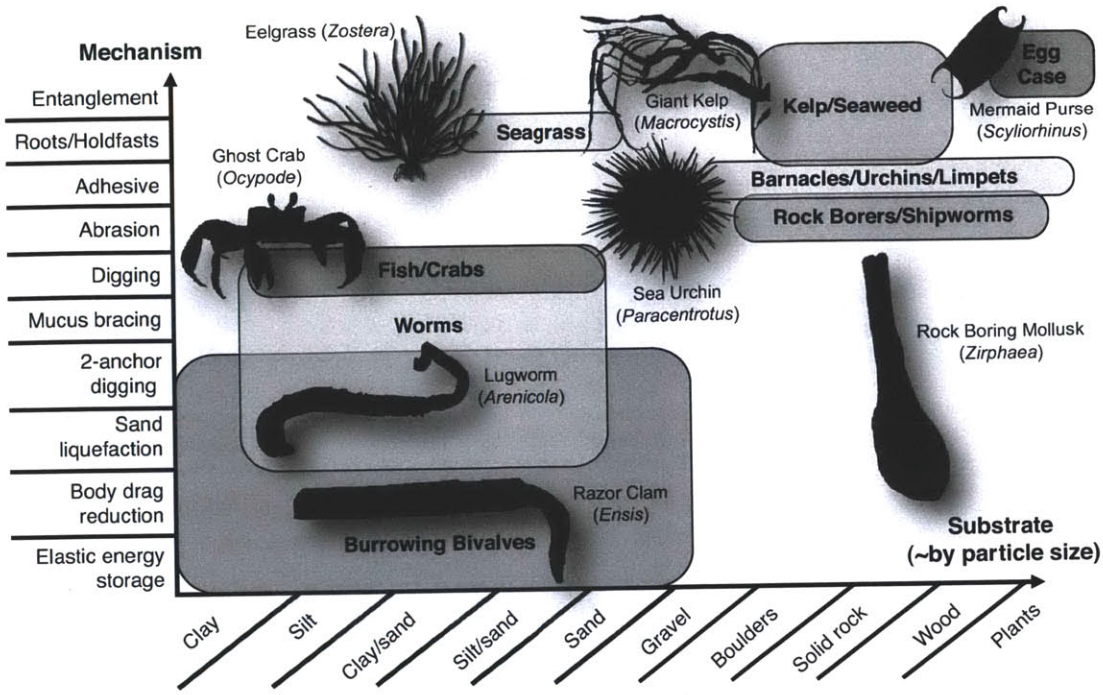

Figure 1-3: Burrowing mechanisms and habitat substrates of undersea animals. Each animal is categorized by its burrowing or anchoring mechanisms (vertical axis) and the substrates in which it lives (horizontal axis). Data for this figure were collected from the following sources: [1, 7, 8, 11, 12, 13, 14, 15, 18, 20, 21, 24, 26, 30, 33, 37, 39, 43, 44, 45, 48, 51, 52, 53, 55, 58, 60, 59, 61, 63, 65, 68, 69, 87, 89, 90, 94, 86, 88, 95, 91, 92, 35, 93, 70, 73, 74, 77, 78, 79, 99, 100, 103]

propagation to burrow in gelatin, a material with similar properties to elastic muds [13]. Smaller organisms, like nematodes (*C. elegans*), have been observed to move efficiently via reciprocating motion in saturated granular media [97, 36].

The hypothesis at the root of this thesis is that nature has found an efficient, compact solution to burrowing into underwater soils. As such, a survey of myriad undersea animals that stick to, cling to, or dig into the ocean bottom was conducted to identify biomimetic candidates. A plot of these animals, the substrates in which they live, and their burrowing/anchoring mechanisms is shown in Fig. 1-3.

Burrowing Bivalves stand out in Fig. 1-3, not only because they live in nearly every type of particulate substrate, but also because they employ burrowing mechanisms to reduce energy expenditure. For example, nearly all bivalves have an elastic ligament that acts as a torsional spring [94], which stores energy during valve contraction to be used for re-expansion.

1.3 Inspiration from *Ensis*

While inspecting biomimetic merits of bivalves, *Ensis directus*, the Atlantic razor clam, stood out for its burrowing performance. *Ensis* is composed of a long, slender set of two valves that rotate relative to each other on an axis oriented longitudinally to the animal. A foot, which is a dexterous, soft organ, resides at the bottom of the valves. *Ensis* burrows by using a series of shell and foot motions to draw itself into the substrate, as shown in Fig. 1-4.

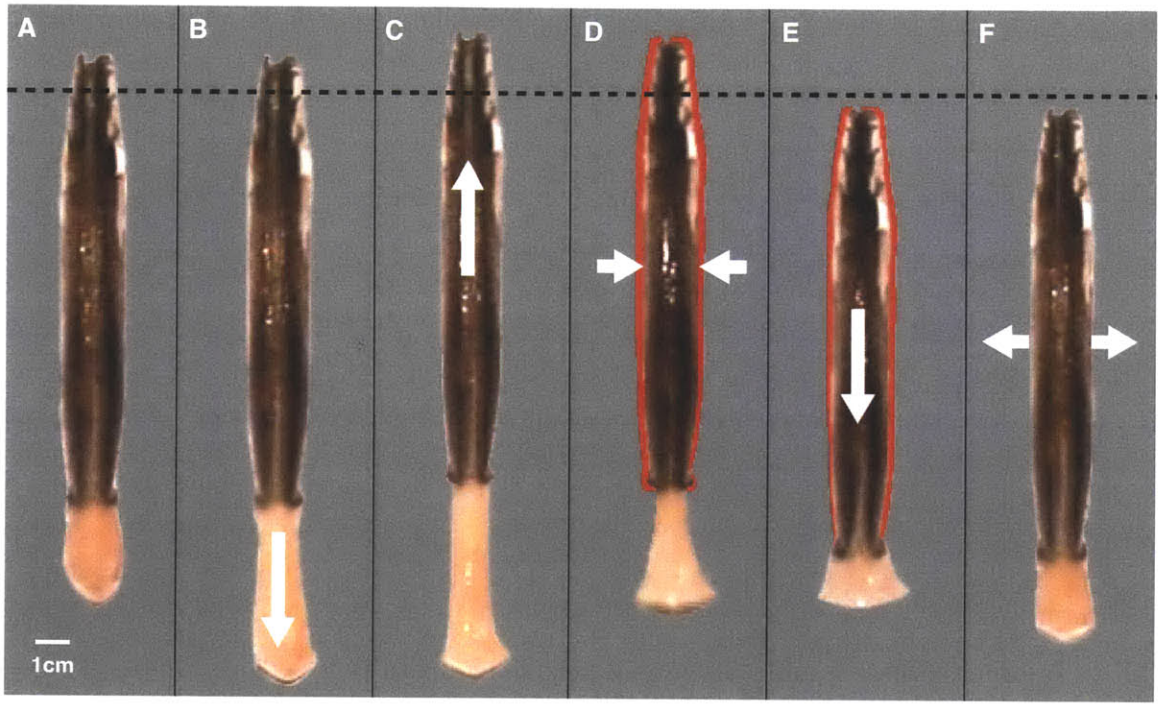

Figure 1-4: *Ensis* kinematics during a burrowing cycle. Dotted line in A)-F) denotes a depth datum. White arrows indicate valve and foot movements. Red silhouette denotes valve geometry in expanded state, before contraction. A) *Ensis* at initiation of digging cycle. B) Extension of foot. C) Valve uplift. D) Valve contraction, which pushes blood into the foot, expanding it to serve as a terminal anchor. E) Retraction of foot and downwards pull on the valves. F) Valve expansion, reset for next digging cycle.

The upper bound of expended mechanical energy per unit depth for *Ensis* to advance its shell into soil was estimated by adapting max pedal strength, valve displacement, hinge stiffness, and mantel cavity pressure values measured by Trueman [90]. For linear motions, energy expended was calculated as $E = F\delta$, where F is the

force acting between the valves and foot and δ is longitudinal valve displacement. Energy expended during rotational actuation of the valves was estimated as $E = T\theta$, where T is the torque developed about the valve hinge from pressure in the mantel cavity of the animal acting on the valves and θ is angular deflection. The resulting expended mechanical energy and attained displacements (positive values of depth indicate further penetration into the soil) for each burrowing motion are: valve uplift (0.05J, -0.5cm), valve contraction (0.07J, 20°), valve penetration (0.20J, 2.0cm), which combine for a total of 0.21J/cm. Re-expansion of the valves is accomplished through elastic rebound of the hinge ligament and thus requires no additional energy input by the animal.

The extremely low amount of energy *Ensis* requires to burrow is attractive for engineering applications. To put 0.21J/cm into perspective, *Ensis* could travel over half a kilometer on the energy in a AA battery [19].

1.4 Comparison of *Ensis* performance to existing technology

Assuming nature always finds the best solution to engineering problems is naive. There are numerous examples of manmade technologies that, either for practicality or efficiency, outperform their biological counterparts. For instance, people decided long ago to smooth the land into roads in order to travel on wheeled vehicles, which are much simpler to engineer than legged systems. Similarly, decoupling propulsion and lift, rather than using a flapping wing system, has worked well for airplanes. The Boeing 747 is just as efficient as any bird when comparing wing loading to weight or weight to cruising speed [83]. Anchoring – one of the principal applications of the research in this thesis – was chosen as the benchmark of comparison to evaluate whether *Ensis* could provide an advantage over currently available technologies.

Figures 1-5A-E show common anchoring technologies. All of these anchor types achieve holding force by transferring loads to the soil through flukes, which extend

from the anchor body to increase the area of the anchor acting on the soil. The vertical pulling force an anchor can withstand can be calculated using

$$F = A(c\bar{N}_c + \Delta\rho g D\bar{N}_q)\left(0.84 + 0.16\frac{B}{L}\right), \tag{1.1}$$

which was empirically-derived [50], where F is anchoring force, c is the cohesive strength of the soil, $\bar{N}_c$ is a cohesive fitting factor, $\Delta\rho$ is the difference in density between the water and soil, g is the gravitational constant, D is the anchor depth in soil, $\bar{N}_q$ is a buoyancy fitting factor, and $\frac{B}{L}$ is the fluke aspect ratio. For scaling purposes, if only granular (non-cohesive) soils are considered, and $\left(0.84 + 0.16\frac{B}{L}\right) \approx 1$ for most fluke shapes, Eq. 1.1 simplifies to

$$F \approx \bar{N}_q \Delta\rho g A D. \tag{1.2}$$

Figure 1-5F shows historical data of max pulling force in sand for anchors of varying size and embedment depth [50]. Using the simplified expression for anchoring force in Eq. 1.2, a least squares fit of these data yields a buoyancy fitting factor of $\bar{N}_q = 6.2$. With this result, the anchoring force of an *Ensis*-based system can be predicted from the animal's burrow depth and valve area, which is approximated as fluke area, as shown in inset a of Fig. 1-5F.

Two metrics were chosen to compare the performance of an *Ensis*-based anchor with current technology. The first is anchoring force developed per unit of insertion energy. This metric would be of particular importance when choosing an anchor for an AUV, where energy is at a premium. Figure 1-6 shows that an *Ensis*-based anchor beats other technologies in force/energy by at least an order of magnitude.

The second metric of comparison is anchoring force per unit device weight. Figure 1-7 shows that an *Ensis*-based anchoring system achieves the same anchoring force for half or less the weight of other technologies. It should be noted that, in reality, many of the existing technologies have a much greater effective weight than what is represented in Fig. 1-7 because of required installation equipment. For example, umbrella piles are hammered into soil with a pile driver and drag anchors require

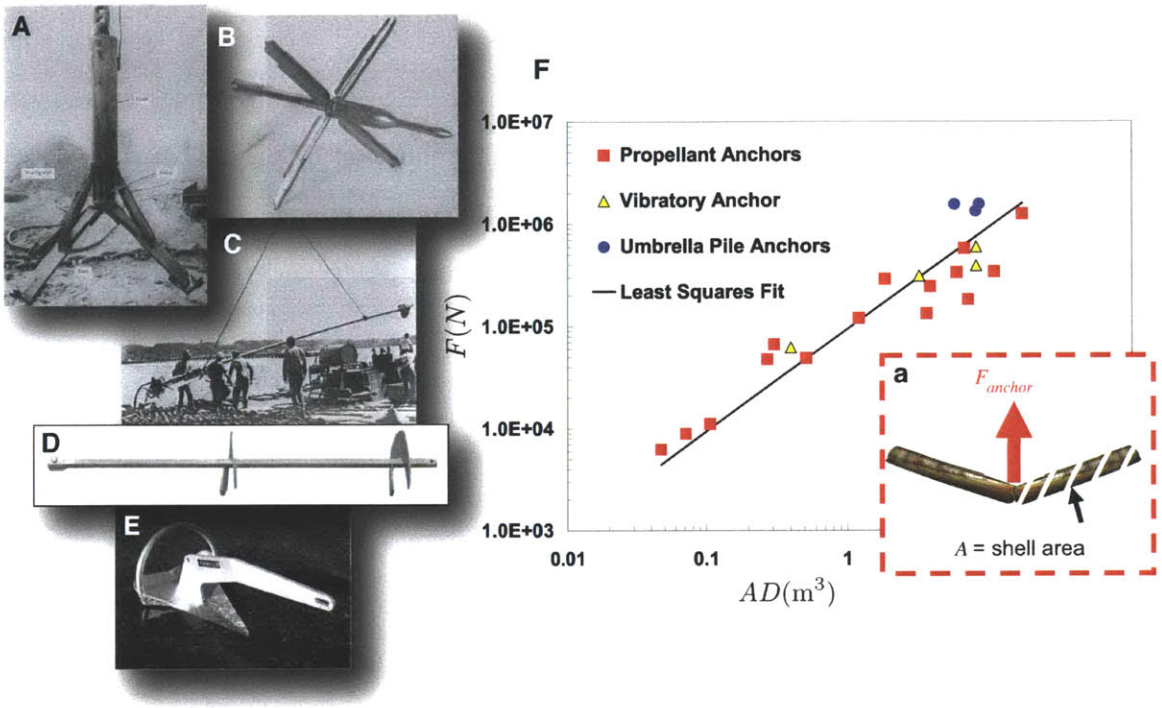

Figure 1-5: Anchor types and their performance. A) Umbrella pile, which is pounded into soil and then secured by folding out the flukes, the arm-like structures at the bottom of the anchor. Picture from [50]. B) Propellent anchor, which is shot into soil like a bullet. The flukes lie parallel with the anchor's body during insertion and then deploy when the anchor is pulled upwards. Picture from [50]. C) Vibratory anchor, which has a vibrating mass at one end that shimmies the fluked end into the soil. Picture from [50]. D) Helical anchor, which is screwed into the soil. Picture from [32]. E) Drag anchor, which has a special fluke and body geometry that forces the anchor to dig into the soil as it is dragged along the ocean floor. Picture from [67]. F) Historical data of various anchor types [50] showing the relationship between anchoring force F, fluke area A, and submerged depth in soil D. Inset a shows the effective fluke area of an *Ensis*-inspired anchor, with orientation similar to a propellant anchor.

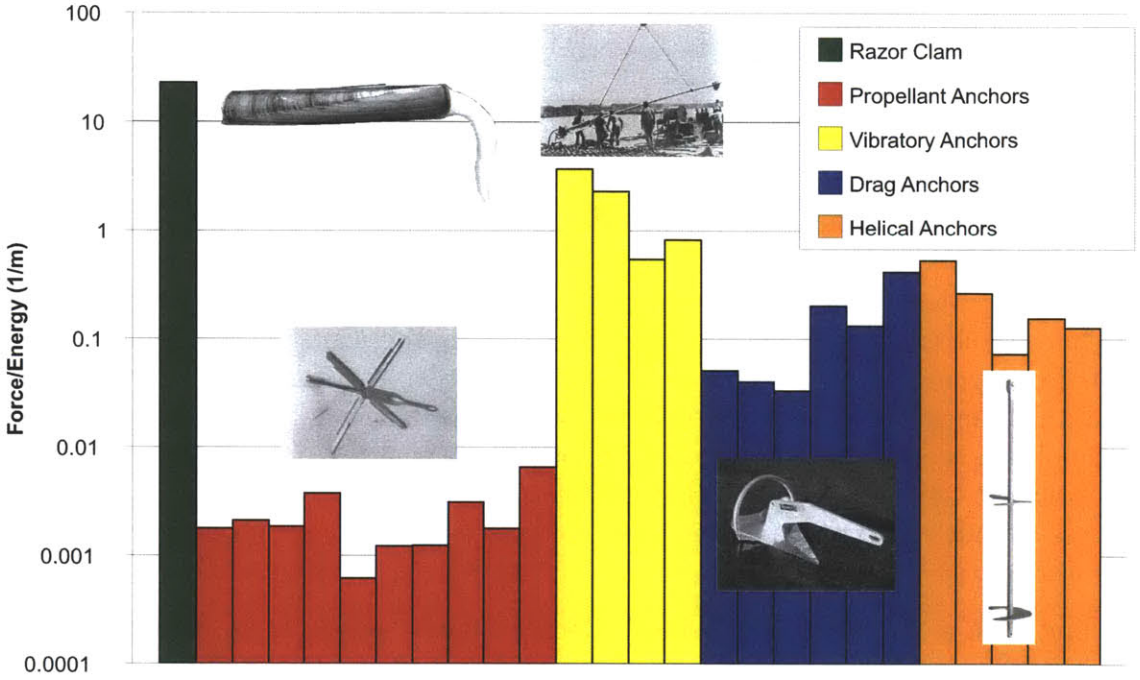

Figure 1-6: Anchoring force developed per unit of insertion energy for an *Ensis*-based anchor versus existing technologies. Performance of the *Ensis*-based system was computed with an energetic expenditure of 0.21J/cm, calculated from [90], and a maximum burrow depth for the animal of 70cm [30]. Performance data of existing anchoring technologies were adapted from [29, 76, 50, 9], with each bar representing an actual historical test. The figure shows that an *Ensis*-based system is predicted to out-perform every technology by at least an order of magnitude.

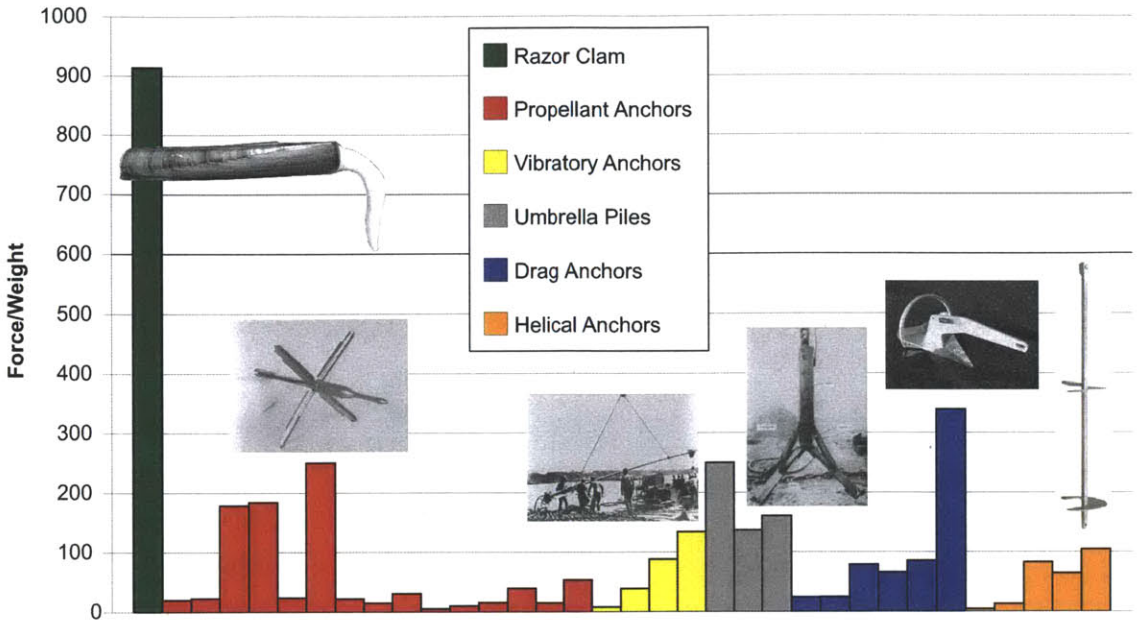

Figure 1-7: Anchoring force developed per unit device weight for an *Ensis*-based anchor versus existing technologies. Performance of the *Ensis*-based system was computed by assuming the device has the same density as water (similar to the animal), and a maximum burrow depth of 70cm [30]. Performance data of existing anchoring technologies were adapted from [29, 76, 50, 9], with each bar representing an actual historic test. The figure shows that an *Ensis*-based system is predicted to weigh half or less as much as other anchoring technologies for a given anchoring force.

pulling from a boat to be embedded. Decreasing the weight of an overall anchoring system is favorable for many reasons, including ease of handling aboard ship and reduction of transportation energy.

1.5 Summary of *Ensis'* engineering merits

The previous section demonstrates how an *Ensis*-based anchoring system may provide significant advantages over currently available technologies. Anchoring was chosen as a basis for comparison, in part, because of applications of interest to the sponsors of this project. In summary, *Ensis* was chosen for the basis of a new biomimetic burrowing technology because it has the following engineering merits:

- **Fast** Burrows at nearly 1cm/s [90].

- **Efficient** Uses approximately $0.21 J/cm$ to advance its body downwards.
- **Large** At 20cm long and 3cm wide, is the size scale of a real engineering device.
- **Simple** Has no brain and presumably no complicated control system. Shell is composed of two rigid valves with a single degree-of-freedom hinge.
- **Digs deep** Burrows up to 70cm, upwards of 7 body lengths for juvenile clams [30].
- **Tech advantage** *Ensis*-based anchoring systems are predicted to be significantly more efficient and lower weight than currently-available technologies.

Chapter 2

Localized fluidization burrowing

This chapter describes how *Ensis* uses motions of its valves to create a pocket of fluidized substrate around its body in order to reduce drag forces and burrowing energy. Localized fluidization around burrowing *Ensis* was measured by tracking the movement of substrate particles using particle image velocimetry (PIV) in a novel visualization system. The PIV data presented here show *Ensis'* uplift and contraction valve motions pull water towards the animal's body and unpack the surrounding soil beyond incipient fluidization, inducing a fluidized state. The formation of the fluidized region within the plain strain condition of the visualizer is explained using constitutive soil and fluid models. Drag force analysis and experimental results show *Ensis* is too weak to burrow in static soil, yet strong enough to move through fluidized substrate. Furthermore, by locomoting through fluidized, rather than static, soil, *Ensis* reduces the amount of energy to reach burrow depth by an order of magnitude with burrowing energy that scales linearly with depth, rather than depth squared.

2.1 *Ensis* collection

Ensis specimens used in this research were collected from natural stocks in Orleans and Gloucester, Massachusetts under the appropriate research collection permit[1].

[1]Commercial Permit: Scientific. Permit ID 152936. Commonwealth of Massachusetts, Department of Fish and Game, Division of Marine Fisheries, 251 Causeway St. No. 400, Boston, MA 02114

Once specimens were harvested and brought back to MIT, they were held in the commercial lobster tank[2] shown in Fig. 2-1, which supplies oxygenated seawater at 10° C – conditions similar those in to coastal Massachusetts. The holding area of the tank is split into two sections, one filled with sand to allow the clams to burrow.

2.2 Visualization of *Ensis* burrowing

The adage clear as mud aptly describes the difficulty of visually investigating burrowing animals *in situ*. To surmount this challenge and view *Ensis* burrowing motions, as well as deformations in the soil surrounding the animal, the visualizer shown in Fig. 2-2A was developed. The tank is essentially a Hele-Shaw cell, commonly used in fluid mechanics experiments to measure flow in two dimensions [41]. The front viewing pane is adjustable forward and aft via a lead screw and bellowed side walls, allowing tank and animal thickness to be matched. Specimens in the tank are visualized in silhouette by three halogen lamps mounted behind the substrate, as shown in Fig. 2-2B.

The substrate used in the visualizer is 1mm diameter, optically clear soda lime glass beads[3]. This substrate was chosen because its density of 2.52 g/cm^3 is close to 2.66 g/cm^3 for real quartz sand [84], one of the substrates in which *Ensis* lives [30]. Through experimentation, it was found that light transmission through the substrate increases with particle size. One millimeter beads were determined to be the best experimental substrate because they fall within the size scale of coarse sand grains [84] and provide adequate visualization of test animals.

Heat dissipation was an important consideration in the visualizer design, as the halogen lamps would melt the walls of the tank (and kill the animals) within minutes if not actively cooled. Fig. 2-2C shows the fluid circuit diagram of the recirculation system in the visualizer. Chilled and oxygenated water is supplied from the lobster tank used to hold specimens. This water is mixed with hot water flowing out of the

[2]Fifty gallon lobster tank. Stark Products. 29-14 122nd Street, College Point, NY 11354

[3]A100 Technical Quality Glass Spheres. Potters Industries. 300 Lindenwood Drive, Valleybrooke Corporate Center, Malvern, PA 19355-1740

Figure 2-1: Lobster tank used to hold *Ensis* specimens. The left side of the tank is filled with sand, to give *Ensis* a place to burrow. The large animal on the right side is a geoduck, a type of burrowing bivalve found in the Pacific Northwest.

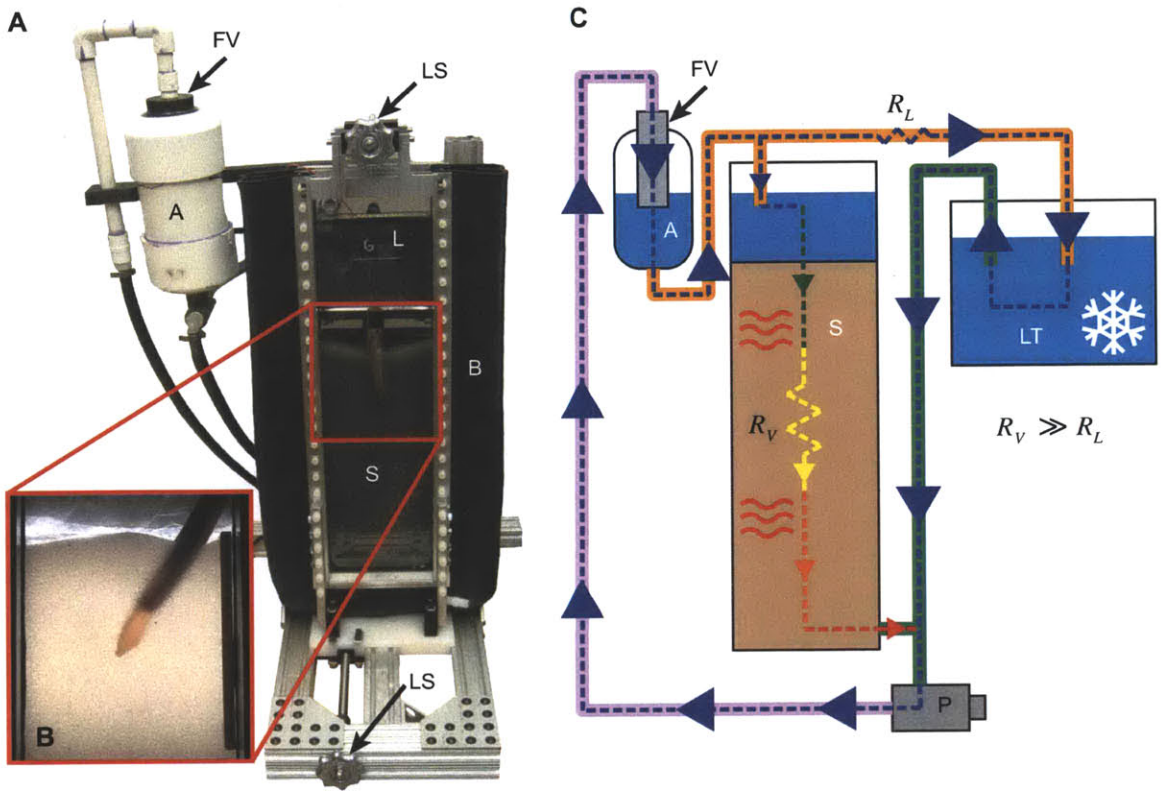

Figure 2-2: Burrowing visualization system. A) Visualization tank filled with 1mm soda lime glass beads. Viewing panes are adjustable via lead screws to match tank and animal width, forcing a plane strain condition. Labeled regions: float valve (FV); accumulator (A); lead screw (LS); 500W halogen light (L); bellowed sidewall (B); and substrate (S). B) Example image of illuminated visualization tank with *Ensis* clearly seen in silhouette. C) Flow diagram of the visualizer's cooling and recirculation system. Chilled water, fed by gravity from a commercial lobster tank (LT), is mixed with warm water from the visualizer and fed into a pump. Water is pumped into the accumulator, which maintains level in the visualizer via a float valve. The outlet from the accumulator feeds both the visualizer and a short circuit line back to the lobster tank. As the resistance through the visualizer, R_V, is much more than the "short circuit" line resistance, R_L, nearly all of the water flowing from the pump is fresh from the lobster tank. The system is able to maintain temperature within 2°C between the visualizer and lobster tank with two halogen lights illuminated.

visualizer and gravity-fed into a pump. The pump sends water to a reservoir with a float valve that maintains fill level near the top of the visualizer. Two outlets leave the reservoir: one into the top of the visualizer, and one directly back to the lobster tank. Because the flow resistance through the substrate within the visualizer is much greater than the resistance of the "short circuit" line from the reservoir to the lobster tank, the portion of heated water that enters the supply stream at the pump is small compared to chilled water from the lobster tank. The cooling system can maintain the visualizer within 2°C of the lobster tank when it is set to 10°C and two halogen lights are illuminated.

2.3 Measurement of soil deformation around burrowing *Ensis*

Opaque particles interspersed in the visualizer substrate were tracked with particle image velocimetry (PIV) [82] during *Ensis* burrowing to quantitatively measure soil deformations. Soils constitutive properties largely depend on void fraction, ϕ, which is the percentage of the substrate's volume occupied by voids (liquid or gas). As such, PIV data was used to calculate the instantaneous void fraction field around *Ensis* with the following method. The instantaneous displacement field, $\partial\delta_i$, can be calculated with

$$\partial\delta_i = v_i dt = \frac{\partial\delta_i}{\partial t} dt, \tag{2.1}$$

where v_i is the velocity field and dt is the change in time between video frames. The volumetric strain field in the soil, e, is calculated by summing the principal strain fields, ϵ_{ii}.

$$e = \epsilon_{11} + \epsilon_{11}, \text{ where } \epsilon_{ii} = \frac{\partial\delta_i}{\partial x_i}. \tag{2.2}$$

Note that the visualizer imposes a plane strain condition, where $\epsilon_{33} = 0$.

The volumetric strain at a point describes the bulk deformation of a differential

element of soil, which can also be written as

$$e = \frac{V_f^t - V_i^t}{V_i^t}, \tag{2.3}$$

where V_f^t is the final and V_i^t is the initial total volume of the element. If the initial volume of solids in the element is V_i^s, then the final volume of solids is given by

$$V_f^s = V_i^s \frac{V_i^t}{V_f^t}. \tag{2.4}$$

Substituting Eq. 2.4 into Eq. 2.4 yields Eq. 2.5, an expression for the current void fraction, ϕ, given the initial void fraction, ϕ_0, and the volumetric strain.

$$e = \frac{V_i^s - V_f^s}{V_f^s} = \frac{V_i^t(\phi - \phi_0)}{V_i^t(1-\phi)} \rightarrow \frac{e + \phi_0}{1+e} = \phi. \tag{2.5}$$

With Eq. 2.5, temporal changes in void fraction around burrowing *Ensis* can be calculated from PIV data. The only initial condition required is the initial void fraction ϕ_0, which is easily calculated by knowing any two of the following: volume of the experimental setup, volume of the pore fluid, or volume of the soil particles. Through experimental calibration of the burrowing visualization setup, which entailed PIV measurement of a soil undergoing a known void fraction change, it was found that a 7% concentration of opaque particles yields the least error in void fraction, which was measured to be $\pm 4\%$.

2.4 Discovery of localized fluidization burrowing

Figure 2-3 shows temporal void fraction changes in the substrate during one *Ensis* burrowing cycle. Data are plotted as the current void fraction divided by the initial void fraction. Areas of color denote regions of unpacking (increase in void fraction) in the substrate. Video frames of burrowing *Ensis* used in the PIV analysis have been laid under the resulting data.

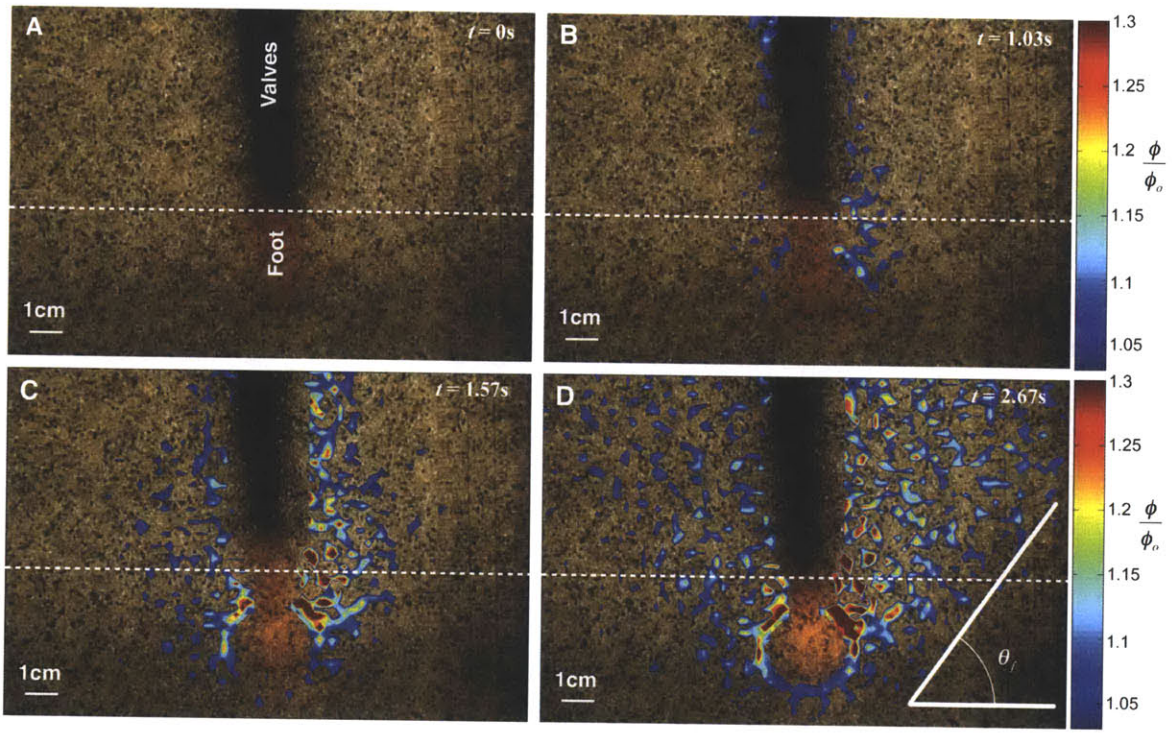

Figure 2-3: PIV results overlaid on video frames showing localized fluidization around burrowing *Ensis*. Dotted line is a depth datum. Fluidization plotted as current void fraction divided by initial void fraction. A) Start of burrowing cycle. B) Valve uplift motion, initiating fluidization below *Ensis*. C) Valve contraction, creating a pocket of fluidized substrate around the animal. D) Foot contraction and downward motion of the valves. The failure wedge, which develops over a longer timescale than initial fluidization by valve contraction, can be clearly seen. Predicted failure wedge angle θ_f, calculated from the soil's friction angle using Eq. 2.11, matches well with the visualized failure wedge.

As can be seen in Fig. 2-3B and C, the uplift and contraction motions of *Ensis* create a tight pocket of unpacked soil around the animals valves. The void fraction within this region varies between approximately 0.42 and 0.46, with an initial void fraction of 0.38. The measured level of unpacking exceeds the void fraction threshold for incipient fluidization of 0.41 for the visualizer's substrate [98]. This means that *Ensis'* valve motions unpack the soil to the extent where particles are no longer in contact, creating a state of fluidization.

Ensis' localized fluidization of the substrate occurs on a timescale smaller than that required for the soil to collapse and fill around the animal. This is shown in Fig. 2-3D, with a clearly defined failure wedge and matching overlaid failure angle θ_f, calculated from the soil's friction angle. This calculation, given by Eq. 2.11, is explained in detail in the following section.

2.5 Mechanics of localized fluidization in a 2D granular substrate

This section is divided into two subsections which describe the principal valve motions *Ensis* uses to locally fluidize soil: valve uplift and valve contraction. It is important to note that the analysis presented here is for an ideally granular (not cohesive) soil in 2D, which reflects the plane strain condition of the visualizer experimental setup in Fig. 2-2. An analysis of localized fluidization in 3D for both cohesive and granular soils, which builds upon the principles presented here, is presented in the following chapter.

2.5.1 Fluidization due to *Ensis* valve uplift motion

A fluidized bed is created when fluid flows upwards (against gravity) through a substrate and the resulting pressure drop, neglecting hydrostatic pressure, supports the weight of the particles. A common example of a fluidized bed is quicksand, where fluid pressure beneath the soil surface is great enough to induce upwards flow and

levitate the substrate particles. The bulk fluid flow velocity (not the flow velocity within the void spaces between particles) to induce fluidization is the same as the settling velocity of a fluidized bed at incipient fluidization. Incipient fluidization is the point of minimum void fraction, ϕ', at which particles lose contact with one another and begin to fluidize. The void fraction at incipient fluidization can be predicted by the relationship developed by Wen and Yu [98],

$$\frac{1-\phi'}{\psi^2(\phi')^3} \cong 11, \tag{2.6}$$

where ψ is the particle shape factor (1 used for round particles).

Richardson and Zaki [64] empirically discovered that the relationship between settling velocity of particles in fluid, v_s, and a single particle's terminal velocity in an infinite fluid, v_t, depends on the void fraction of the mixture raised to the power n.

$$v_s = v_t \phi^n. \tag{2.7}$$

Khan and Richardson [38] determined the correlation between the void fraction exponent in Eq. 2.7 and the Archimedes number, Ar, which is a dimensionless number that relates to the motion of fluids due to differences in density, as

$$\frac{4.8-n}{n-2.4} = 0.043\mathrm{Ar}^{0.57}, \tag{2.8}$$

where $Ar = \frac{g d_p^3 \rho_f (\rho_p - \rho_f)}{\mu_f^2}$, g is the gravitational constant, d_p is the particle diameter, ρ_f is the density of the fluid, ρ_p is the density of the particle, and μ_f is the fluid viscosity. The particle terminal velocity can be defined in terms of the Reynolds number, $\mathrm{Re}_{p,t}$, as

$$v_t = \frac{\mathrm{Re}_{p,t}\mu_f}{\rho_f d_p}. \tag{2.9}$$

The Reynolds number of a sphere at terminal velocity can, in turn, be calculated regardless of whether the flow is dominated by viscous or inertial effects by using the

following correlation to the Archimedes number [25].

$$\mathrm{Re}_{p,t} = \left[-3.809 + \left(3.809^2 + 1.832\mathrm{Ar}^{0.5}\right)^{0.5}\right]^2. \tag{2.10}$$

Equation 2.10 results from the variation in coefficient of drag on a sphere as a function of Reynolds number.

Combining Eqs. 2.6-2.10 enables the settling velocity, and thus the required bulk upward fluid flow velocity, to be calculated at the incipient fluidization packing fraction. The fluidization velocity for 1mm soda lime glass beads is 1.35cm/s. *Ensis'* uplift velocity, measured by Trueman [90], is 1.25cm/s, and the uplift velocity measured during the experiment shown in Fig. 2-3 is 1.05 ± 0.5cm/s. This means *Ensis'* uplift motion induces a velocity in the pore fluid on the order of the velocity required to fluidize the substrate below the animal. Furthermore, 1mm is near the upper bound of particle size in *Ensis* habitat [30]; using the same uplift velocity, *Ensis* can easily fluidize smaller particles. For example, spherical 0.5mm soda lime glass beads will fluidize at a flow velocity of 0.5cm/s.

2.5.2 Fluidization due to *Ensis* valve contraction

As *Ensis* contracts its valves, it reduces the level of stress acting between the valves and the surrounding soil. At some stress level, the imbalance between horizontal and vertical stress causes the soil adjacent to the animal to fail. Continued valve contraction draws pore water towards the animal, which mixes with the failed soil to create a region of localized fluidization.

The stress state in a soil at equilibrium and failure are shown as Mohrs circles [28] in Fig. 2-4. Failure occurs when the internal shear stress in the soil equals its shear strength. Graphically, this is represented when circle b in Fig. 2-4 is tangent to the failure envelope formed by the soil's friction angle φ [84]. The stress state in Fig. 2-4 relates to a cohesionless soil; for a cohesive soil, the same failure analysis can be used, but the failure envelope will be shifted vertically by half the soil's cohesive strength. Each stress shown in Fig. 2-4 is an effective stress [84], which is the total stress in

the soil minus the pore water hydrostatic pressure $u = \rho_f g z$ (where z is total water depth), as to represent the actual stress acting between soil particles.

When *Ensis* first starts to contract its valves, it brings the soil to a state of failure. At this point, the soil will tend to naturally landslide downward at a failure angle θ_f, illustrated by inset b in Fig. 2-4. The failure angle is the transformation angle between the principal stress state and the stress state at the tangency point between the Mohr's circle and failure envelope. This angle can also be seen by connecting the tangency point on the stress envelope, the horizontal effective stress at failure, σ'_{hf}, and the principal stress axis, as shown in Fig. 2-4 and given by Eq. 2.11.

$$\theta_f = \frac{\pi}{4} + \frac{\varphi}{2} \tag{2.11}$$

If *Ensis* contracted its valves slowly, the soil would naturally landslide towards the animal, possibly without unpacking. But *Ensis* does not contract its valves slowly; contraction occurs at a smaller timescale than the natural landslide failure of the substrate, which is clearly seen by comparing Figs. 2-3B-C with Fig. 2-3D. This gives *Ensis* a chance to fluidize the soil before it collapses. The calculated failure angle in the visualizer substrate, determined by measuring the friction angle of 1mm soda lime glass beads to be 25°, is shown in Fig. 2-3D and matches well with the observed failure wedge.

Although bulk landslide movement of the soil does not occur when *Ensis* initiates valve contraction, the resulting imbalance in stresses brings the soil to a state of failure, creating a failure surface at angle θ_f. This is important because the failure surface provides a discontinuity in the surrounding substrate, where soil particles within are free to move and soil particles beyond remain stationary. As *Ensis* contracts its valves, it reduces its own body volume. This change in volume must be compensated by pore fluid drawn into the region around the animal. Movement of the pore fluid will cause drag on, and thus movement of, the surrounding particles, creating a fluidized zone within the failure wedge.

The Reynolds number of valve contraction fluid flow, calculated from *Ensis'* valve

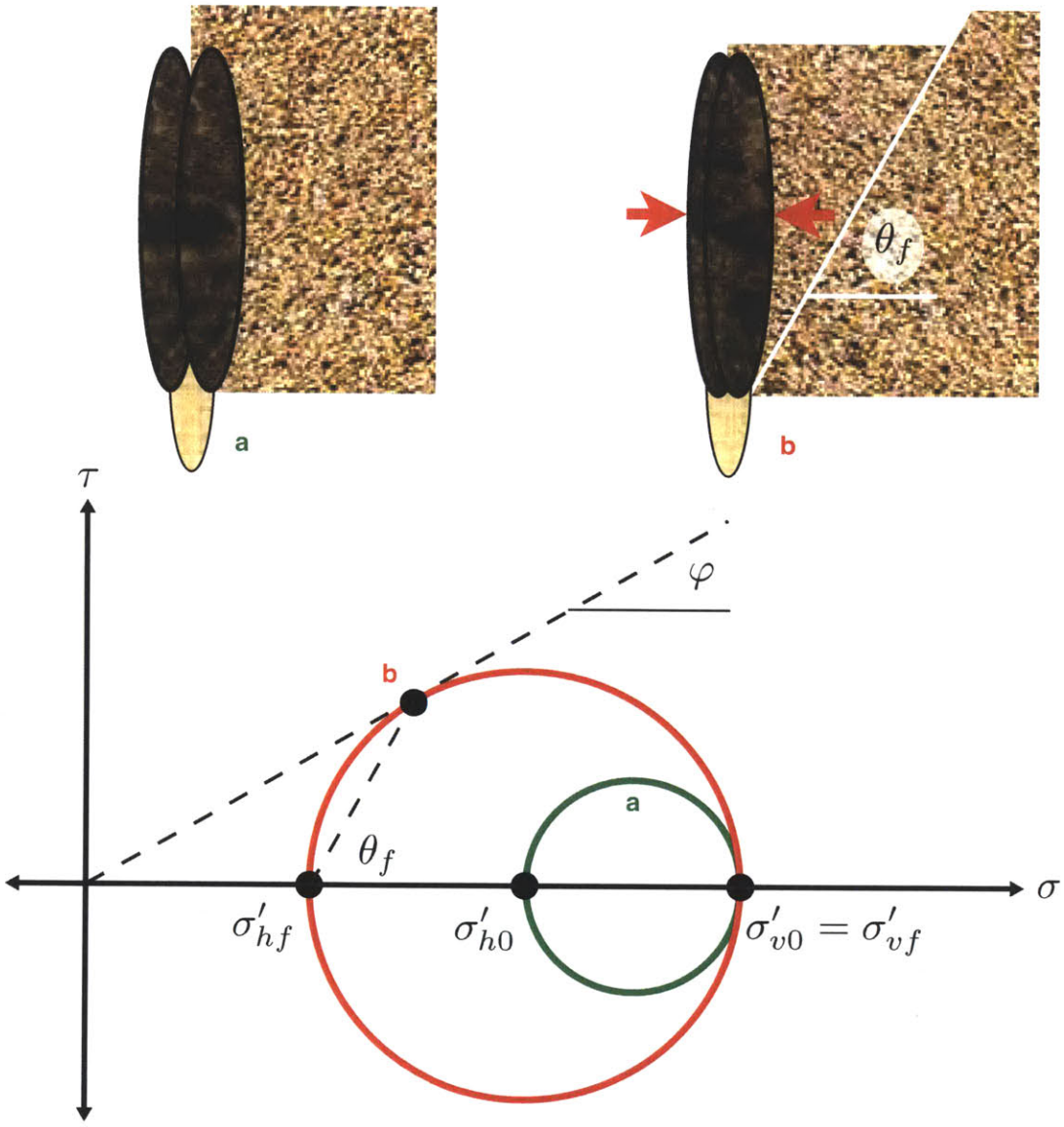

Figure 2-4: Induced soil failure by valve contraction. Mohrs circle and corresponding insets of *Ensis'* interaction with the substrate for equilibrium (a) and active failure (b) stress states. Inset b shows the formation of a failure surface at angle θ_f and the tendency of soil to naturally landslide during valve contraction. Symbols: τ is shear stress; σ is normal stress; subscript h indicates horizontal stress; subscript v indicates vertical stress; subscript 0 indicates equilibrium state; subscript f indicates failure state; and prime denotes effective stresses (i.e. particle contact stress only, without pore water pressure).

velocity, particle diameter, and the pore fluid density and viscosity, varies anywhere between 0.02 and 56, depending on particle size (0.002 to 2mm [90, 30, 84]), animal size (10 to 20cm[4]), and valve contraction velocity (v $\approx$ 0.011 to 0.028m/s [90]). As this range mostly falls within the regime of Stokes drag, but also nudges the lower limits of form drag, which begins at Re $\approx 10^2$ to 10^3 [41], the timescales for a 1mm soda lime glass particle to reach the valve velocity during contraction using conservation of momentum are

$$m_p \frac{dv_p}{dt} = 6\pi\mu_f d_p(v_v - v_p) \rightarrow t_{char} = \frac{d_p^2 \rho_p}{36\mu_f} \tag{2.12}$$

for Stokes drag and

$$m_p \frac{v_v}{\Delta t} \approx \frac{1}{2}\rho_f A_p C_D v_v^2 \rightarrow \Delta t \approx \frac{4 d_p \rho_p}{3\rho_f C_D v_v} \tag{2.13}$$

for form drag, where m_p is the mass of the particle, v_v is the velocity of a contracting valve, v_p is the particle velocity, t_{char} is the time constant of the differential equitation governing velocity change in Stokes flow, A_p is the frontal area of the particle, C_D is the particles coefficient of drag, and Δt is the change in time of the linearized conservation of momentum equation for form drag.

This analysis yields timescales of 0.075s for Stokes drag and 0.27s for form drag for 1mm soda lime glass beads in water. These timescales are less than or on the order of the $\approx$ 0.2s valve contraction time measured by Trueman [90]. Furthermore, 1mm particles are large for *Ensis* habitat; the timescale mismatch is even greater for smaller substrate particles. As such, soil particles surrounding *Ensis* can be considered inertialess and to move directly with the pore fluid during valve contraction. This means particles within the failure wedge are free to mix with the influx of pore fluid caused by *Ensis'* volumetric contraction, whereas the particles outside of the wedge will remain stationary. The discontinuity created by the failure wedge surface is

[4]from experimental observation

critical to achieving localized fluidization, as without the wedge, substrate particles would freely follow the fluid flow field, which is incompressible and governed by $\nabla \cdot \overline{v} = 0$. No divergence in the flow field would create no divergence between particles, and thus no unpacking. The net result of additional pore fluid added to the failure wedge without a flux in particles across the failure surface is an increase in void fraction, as demonstrated by the data in Fig. 2-3.

2.6 Burrowing drag force and energy reductions due to localized fluidization

Trueman measured 10.8N as the maximum pulling force *Ensis* could exert with its foot to pull its valves into the substrate [90]. In experiments conducted with the apparatus shown in Fig. 2-5A, *Ensis'* max pulling force was measured to be as high as 5.6N. To contrast *Ensis'* strength with drag forces experienced by the animal, the blunt body experimental setup shown in Fig. 2-5B, affectionately called the "Clamcicle," was constructed to measure burrowing resistance in static soil. Blunt body penetration tests in *Ensis* habitat off the coast of Gloucester, MA showed 10N of force should enable the animal to submerge to approximately 1-2cm. In reality, razor clams dig to 70cm [30][5]. Since drag force scales linearly with depth for a body moving through a granular medium [66], *Ensis* should be approximately 75X too weak to reach full burrow depth in static soil.

Localized fluidization provides a probable explanation for how *Ensis* reduces burrowing drag forces to within its strength capabilities, as force chains, which give static soil its compressive strength [46], cannot be transferred between particles that are in a fluidized state. Many models exist that describe particle-fluid mixtures as Newtonian fluids, with effective viscosities that increase from the pore fluid's viscosity as a function of void fraction. Einstein was the first to describe this relationship for dilute mixtures as $\mu_{eff} = \mu_f[1 + 2.5(1 - \phi)]$, where μ_{eff} is the mixture's effective viscosity

[5] [30] relates the stout razor clam (*T. plebeius*); burrowing depths on this order have also been observed by the author while collecting *Ensis* in Gloucester, MA.

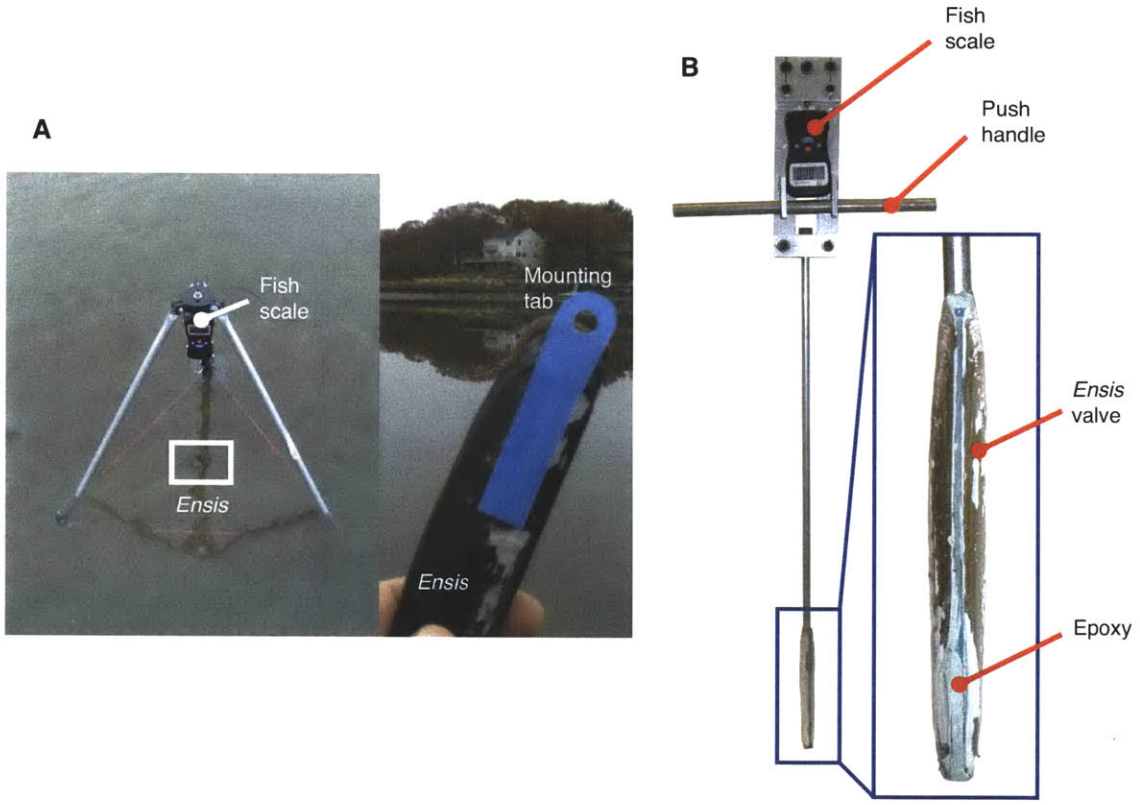

Figure 2-5: Experimental hardware to measure burrowing forces and drag experienced by *Ensis*. A) Experimental setup used to measure *Ensis'* maximum pulling force. The setup is composed of a tripod with a fish scale on top. Fishing line connects the fish scale to a mounting tab, which is adhered to one of *Ensis'* valves. As *Ensis* pulls on the line, the pulling force is read from the fish scale. B) "Clamcicle" blunt body drag measurement device. The end of the device is made from real *Ensis* valves in their natural configuration, adhered to an aluminum rod. Pushing the device into soil gives a measure of drag forces experienced by *Ensis* if it were to burrow in static substrate. Force measurements are read from the fish scale.

[17]. In more recent years, the following empirically-derived equations have been used to model the viscosities of mixtures with smaller void fractions.

Frankel and Acrivos, 1967 (F&A) [23]

$$\mu_{eff} = \mu_f \left(\frac{9}{8}\right) \frac{\left(\frac{1-\phi}{1-\phi_m}\right)^{\frac{1}{3}}}{1 - \left(\frac{1-\phi}{1-\phi_m}\right)^{\frac{1}{3}}} \tag{2.14}$$

Krieger and Dougherty, 1959 (K&D) [40]

$$\mu_{eff} = \mu_f \left(1 - \frac{1-\phi}{1-\phi_m}\right)^{-2.5\phi_m} \tag{2.15}$$

Eilers, 1941 and Ferrini et al., 1979 (E+F) [16, 22]

$$\mu_{eff} = \mu_f \left[1 + \frac{1.25(1-\phi)}{1 - \frac{1-\phi}{1-\phi_m}}\right]^2 \tag{2.16}$$

Maron and Pierce (M&P) [49]

$$\mu_{eff} = \mu_f \left(1 - \frac{1-\phi}{1-\phi_m}\right)^{-2} \tag{2.17}$$

In Eqs. 2.14-2.17, ϕ_m corresponds to the minimum possible void fraction in a fluidized state, which occurs at incipient fluidization.

Since a particle/fluid mixture can be modeled as a Newtonian fluid, with an effective density and viscosity, the drag force acting on *Ensis'* valves as the animal moves through a fluidized substrate can be predicted. Figure 2-6A shows the flow fields around *Ensis'* body as it moves through a burrow of fluidized substrate. For simplicity, *Ensis'* body is modeled as a cylinder.

The resulting flow field around burrowing *Ensis* as its moves its valves downwards

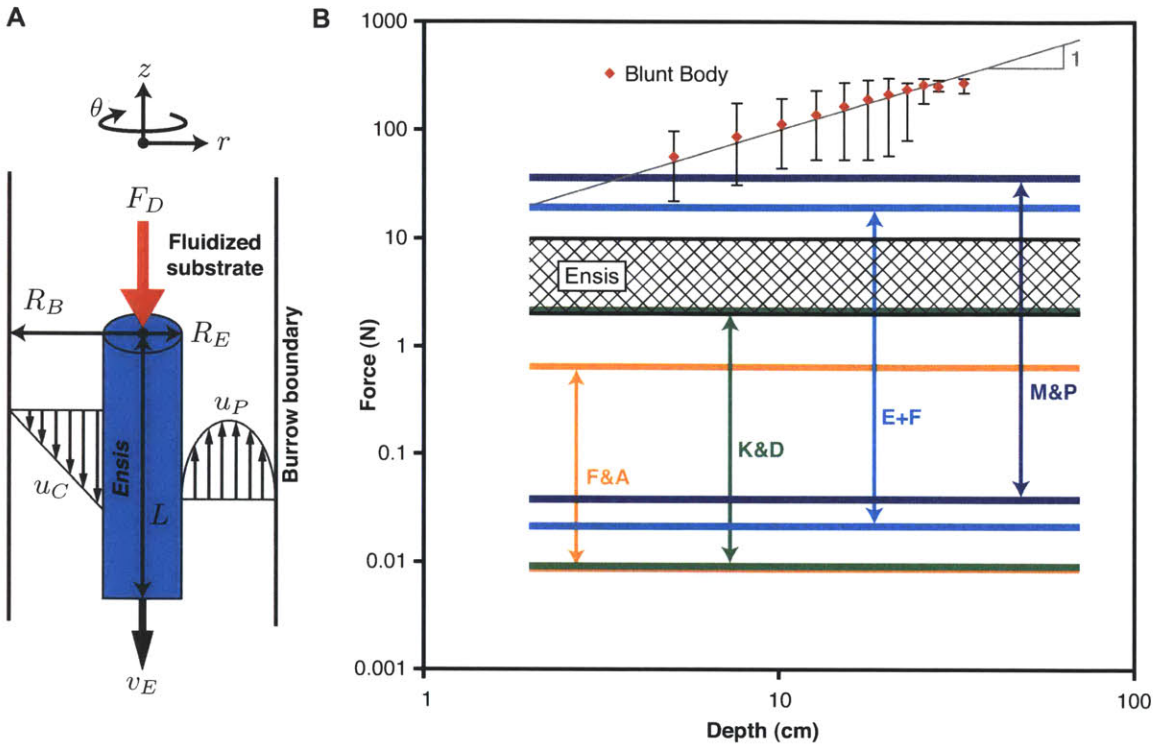

Figure 2-6: Drag force comparison of *Ensis* in fluidized and static substrates. A) Model of fluidized substrate flow around *Ensis* during downwards valve motion. Total flow around the animal is the sum of Couette (u_C) and Poiseuille (u_P) flow fields. Variables: pulling force between valves and foot (F_D), which is equal to drag force; burrow radius (R_B); *Ensis* radius (R_E); *Ensis* length (L); and *Ensis* downwards velocity (V). B) Plot of drag forces on *Ensis* in fluidized and static soil. Crosshatched region denotes *Ensis'* actual pulling force capabilities. Blunt body (Clamcicle) data collected over 16 trials in static soil in *Ensis* habitat using the instrument in Fig. 2-5. Drag force ranges in fluidized substrate calculated with the effective viscosity models in Eqs. 2.14-2.17 and the upper and lower void fraction and burrow size limits measured from data in Fig. 2-3. The plot shows that, although *Ensis* is not strong enough to move through static substrate, drag forces experienced in fluidized substrate are within the animal's strength capabilities and enable it to reach burrow depth.

through fluidized substrate is composed of summed Couette (u_C) and Poiseuille (u_P) flows in an annulus, which are represented separately in Fig. 2-6A. These flow fields can be summed to obtain the total flow field as long as they satisfy the boundary conditions and conservation of mass. Equations for each flow field can be solved by starting with the Navier-Stokes equation for flow in the z-direction in cylindrical coordinates [41].

$$\rho_{eff}\left(\frac{\partial u_z}{\partial t}+u_r\frac{\partial u_z}{\partial r}+\frac{u_\theta}{r}\frac{\partial u_z}{\partial \theta}+u_z\frac{\partial u_z}{\partial z}\right)= \frac{-\partial p}{\partial z}+\mu_{eff}\left[\frac{1}{r}\frac{\partial}{\partial r}\left(r\frac{\partial u_z}{\partial r}\right)+\frac{1}{r^2}\frac{\partial^2 u_z}{\partial \theta^2}+\frac{\partial^2 u_z}{\partial z^2}\right]+\rho_{eff}g_z. \tag{2.18}$$

In Eq. 2.18, r, θ, and z correspond to the three principal directions in Fig. 2-6A, u is velocity, ρ_{eff} and μ_{eff} are the effective density and viscosity, respectively, of the fluid/particle mixture, p is the pressure driving the Poiseuille flow, and g_z is the acceleration due to gravity in the z-direction.

The Poiseuille velocity field is found by reducing Eq. 2.18 with the assumptions that the flow is in steady state (i.e. no changes in time), there is no flow in the r and θ-directions, the flow field does not vary over the length of the valves (i.e. infinitely-long body assumption) or in the θ-direction, and hydrostatic pressure changes do not affect drag on the body. These simplifications yield

$$\frac{d}{dr}(r\mu_{eff}\frac{du_P}{dr})=\frac{dp}{dz}. \tag{2.19}$$

Integrating Eq. 2.19 and applying the appropriate boundary conditions of $u_p\big|_{r=R_E} = u_p\big|_{r=R_B} = 0$ yields the Poiseuille component of the flow field in the annulus around burrowing *Ensis*.

$$u_P=\frac{1}{4\mu_{eff}}\frac{-dp}{dz}\left[R_B^2-r^2+\frac{R_B^2-R_E^2}{\ln\left(\frac{R_E}{R_B}\right)}\ln\left(\frac{R_B}{r}\right)\right]. \tag{2.20}$$

The Couette velocity field is found by reducing Eq. 2.18 with the assumptions

that the flow is in steady state (i.e. no changes in time), there is no flow in the r and θ-directions, the flow field does not vary over the length of the valves (i.e. infinitely-long body assumption) or in the θ-direction, and there is no pressure driving the flow. These simplifications yield

$$\frac{d}{dr}\left(r\frac{du_C}{dr}\right) = 0. \tag{2.21}$$

Integrating Eq. 2.21 and applying the appropriate boundary conditions of $u_C\big|_{r=R_E} = -v_E$, where v_E is *Ensis'* downward velocity, and $u_C\big|_{r=R_B} = 0$, yields the Couette component of the flow field in the annulus around burrowing *Ensis*.

$$u_C = \frac{v_E}{\ln\left(\frac{R_E}{R_B}\right)} \ln\left(\frac{R_B}{r}\right). \tag{2.22}$$

From conservation of mass, the volume of fluidized substrate displaced per unit time by *Ensis* as it moves downward through the burrow must equal the volumetric flow rate of fluid/particle mixture pushed upwards past the animal's body. This relationship is expressed as

$$\pi R_E^2 v_E = \int_{R_E}^{R_B} (u_P + u_C) 2\pi r dr. \tag{2.23}$$

Evaluating the integral in Eq. 2.23 yields an expression for $\frac{dp}{dz}$, the pressure differential driving the Poiseuille flow. Once this differential is known, the total drag force (F_D) acting on *Ensis* is solved by summing the forces caused by the pressure differential (F_{press}) and skin friction (F_{skin}) acting on the body, where L is the body's length.

$$\begin{aligned} F_D &= F_{press} + F_{skin} \\ &= \pi R_E^2 \frac{-dp}{dz} L + 2\pi R_E L \mu_{eff} \frac{d}{dr}(u_P + u_C)\Big|_{r=R_E}. \end{aligned} \tag{2.24}$$

Fig. 2-6B juxtaposes *Ensis'* pulling strength capabilities with Clamcicle forces in static substrate and fluidized soil drag forces calculated using Eq. 2.24 for different viscosities predicted by Eqs. 2.14-2.17. The upper bound of *Ensis* pulling capability was measured by Trueman [90] and the lower bound with the experimental setup in Fig. 2-5A. Clamcicle data was collected over 16 trials in real *Ensis* habitat off Gloucester, MA using the instrument in Fig. 2-5B. Parameters for the drag force models were taken from data shown in Fig. 2-3 and Trueman's maximum measured downward velocity for *Ensis* of 10cm/s [90]. The variation in fluidized substrate drag force is due to: a) the burrow radius varies between two and four times the radius of *Ensis*; and b) the measured void fraction is between 0.42 and 0.46. The results in Fig. 2-6 show that although *Ensis* is too weak to move through static soil, moving through fluidized soil lowers drag forces to within the animals strength capability and enables it to reach burrow depth.

Ensis burrowing energetics adapted from Trueman [90] are plotted in Fig. 2-7 against blunt body (Clamcicle) energetics calculated using $E = \int F dz$ from force data in Fig. 2-6B. The figure shows that moving through fluidized, rather than static, soil reduces the amount of energy *Ensis* has to expend to reach full burrow depth by an order of magnitude. Furthermore, because *Ensis* moves through a fluidized medium, the drag force on its body should ideally remain constant with depth. In contrast, moving through a static particulate medium, as in the case of the Clamcicle, requires pushing force that increases linearly with depth [66]. This means *Ensis* reduces burrowing energy from scaling with depth squared to linearly increasing with depth, even though there is an energetic cost associated with locally fluidizing the soil.

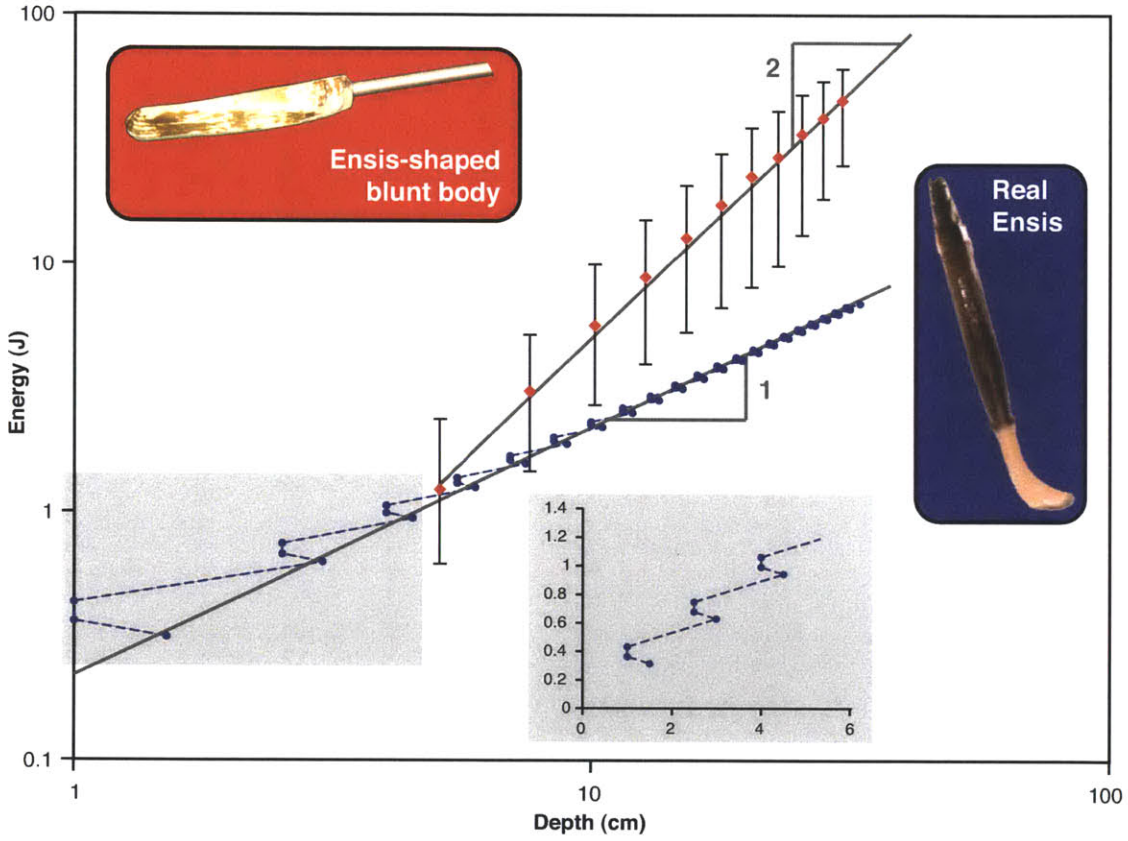

Figure 2-7: Energetic savings achieved via localized fluidization burrowing. The blunt body (Clamcicle) in Fig. 2-5B requires an order of magnitude more energy to reach full burrow depth than real *Ensis*. Using localized fluidization, burrowing energy scales linearly with depth, rather than depth squared for moving through static soil.

Chapter 3

The mechanics of localized fluidization in 3D

This chapter provides a theoretical and experimental explanation for how *Ensis* creates a pocket of fluidized soil around its body within a 3D bed of soil. The previous chapter focused on observations of localized fluidization and the mechanisms behind its occurrence when induced in the 2D, plane strain setup of the visualizer in Fig. 2-2. *Ensis'* valve contraction creates a stress imbalance in the surrounding soil, which leads to the formation of a local failure surface. As the animal contracts its valves, the the soil within the failure surface is free to fludize, wherease the soil outside remains static. This chapter extends upon the failure-fluidization concept, with theory to describe the formation of a failure surface in 3D using a combination of fluid, solid, and soil mechanics with geotechnical soil parameters. Analytical and experimental results show that soil failure will occur within four characteristic lengths from a contracting body, independent of whether the soil is granular or cohesive.

3.1 Failure surface formation around a contracting cylindrical body

When the *Ensis* contracts its valves, it reduces the pressure acting between its body and the adjacent substrate. The resulting imbalance between vertical and horizontal soil stresses causes the soil to fail. This scenario can be expressed with a simplified model of a cylinder with contracting radius that is embedded in saturated soil, as shown in Fig. 3-1.

To neglect end effects, *Ensis* is modeled as an infinitely long cylinder. Furthermore, if the animal's depth is considered much greater than its length ($h \gg L$), stresses acting on the valves can be considered uniform. When *Ensis* initiates valve contraction, it will induce changes in soil stress, causing incipient failure without yet moving the substrate particles. As this relaxation in pressure can be considered quasi-static, and static soil can be modeled as an elastic solid [84], stresses due to inertial effects can be ignored and the radial and hoop stress distribution in the substrate can be described with thick-walled pressure vessel equations [85].

$$\sigma_r = \frac{a^2 b^2 (p_0 - p_i)}{b^2 - a^2} \frac{1}{r^2} + \frac{p_i a^2 - p_0 b^2}{b^2 - a^2}. \tag{3.1}$$

$$\sigma_\theta = -\frac{a^2 b^2 (p_0 - p_i)}{b^2 - a^2} \frac{1}{r^2} + \frac{p_i a^2 - p_0 b^2}{b^2 - a^2}. \tag{3.2}$$

In Eqs. 3.1 and 3.2, σ_r is radial stress, σ_θ is hoop stress, a is the inner radius of a generalized pressure vessel, b is the outer radius, p_i is the inner pressure, and p_0 is the outer pressure. A positive pressure exerts a compressive load, and a compressive stress is negative. It is important to note that these equations still hold if there is a body force acting in the z-direction, such as in soil. In this case, the pressure vessel equations describe the state of stress within annular differential elements stacked in the z-direction.

If *Ensis* is considered to be in an infinite bed of soil in the lateral directions, b can be considered infinite. Applying this condition and reversing signs to geotechnical

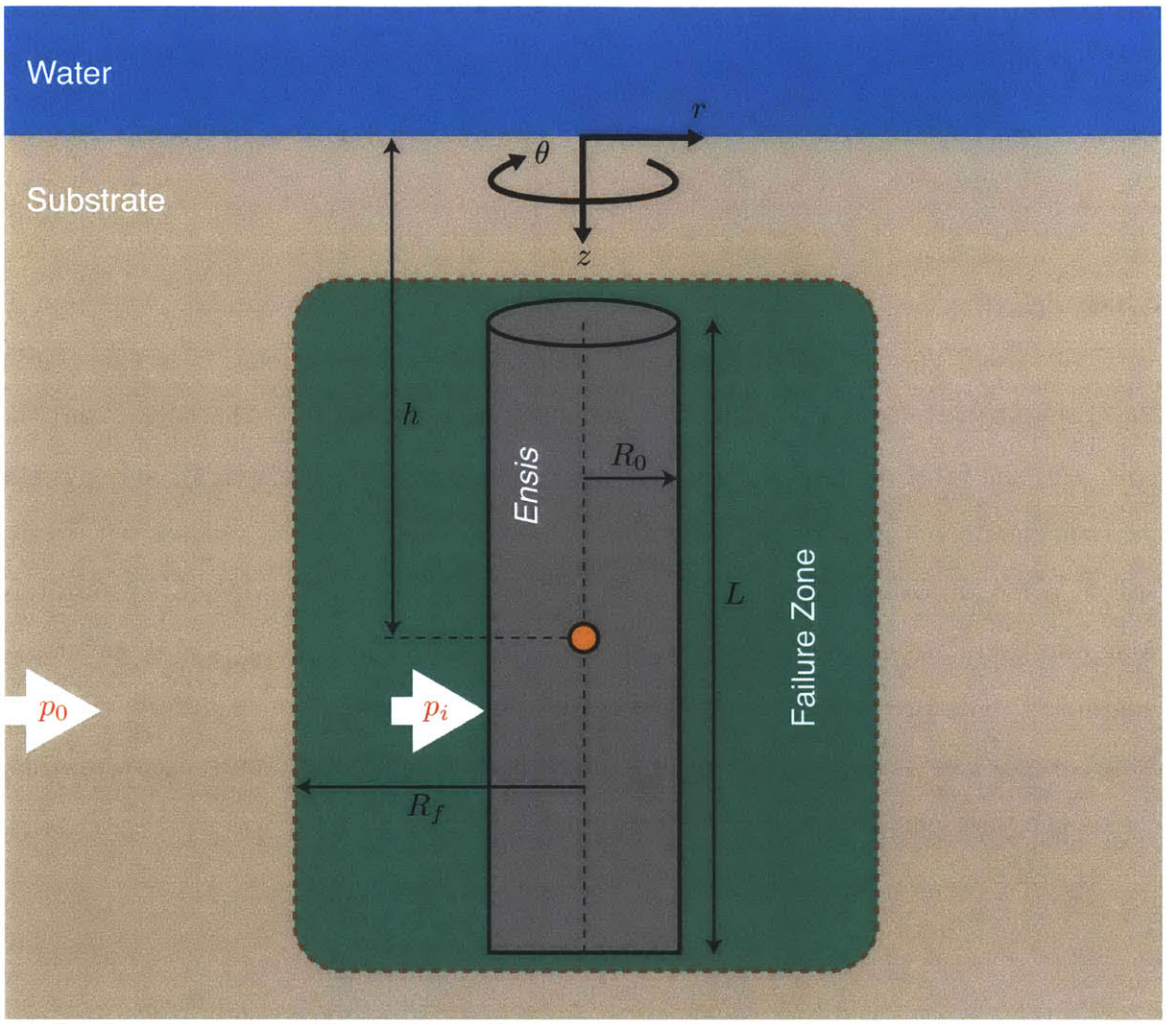

Figure 3-1: Simplified, cylindrical model of soil failure around contracting *Ensis*. As *Ensis* contracts its valves, it reduces the pressure acting between its body and the soil, p_i, below that of the equilibrium lateral soil pressure, p_0. This stress imbalance induces a localized failure zone around the animal. Labels: r, z, and θ denote the coordinate system; h is *Ensis'* depth in the substrate; L and R_0 are the animal's length and expanded radius, respectively; and R_f is the radius of the failure zone.

conventions (with compressive stresses positive) results in

$$\sigma_r = \frac{R_0^2(p_i - p_0)}{r^2} + p_0, \tag{3.3}$$

$$\sigma_\theta = -\frac{R_0^2(p_i - p_0)}{r^2} + p_0, \tag{3.4}$$

$$\text{and } \sigma_z = \rho_t g h, \tag{3.5}$$

which describe the full state of stress in the soil around the animal, where σ_z is vertical stress, R_0 is *Ensis'* expanded radius (before contraction), h is the clam's depth beneath the surface of the soil, p_i is the pressure between the valves and the soil, ρ_t is the total density of the substrate (including solids and fluids), and g is the gravitational constant. It should be noted that there are no shear stresses within the soil in principal orientation, as $\tau_{rz} = \tau_{\theta z} = 0$ because *Ensis* is modeled as infinitely long and there are no shear stresses acting on the soil surface, and $\tau_{r\theta} = 0$ because of symmetry. The pressure p_0 is the total lateral earth pressure at an infinite distance away from *Ensis*. This pressure minus the pore fluid hydrostatic pressure, $u = \rho_f g h$, yields the undisturbed horizontal effective stress

$$\sigma'_{h0} = p_0 - u, \tag{3.6}$$

which is the actual stress acting between soil particles. Likewise, the undisturbed vertical stress is found by subtracting the pore fluid hydrostatic pressure from the total vertical stress.

$$\sigma'_{v0} = \sigma_z - u. \tag{3.7}$$

The undisturbed horizontal and vertical effective stresses can be correlated through

$$K_0 = \frac{\sigma'_{h0}}{\sigma'_{v0}}, \tag{3.8}$$

where K_0 is the coefficient of lateral earth pressure (also sometimes referred to as the coefficient of earth pressure at rest, coefficient of lateral stress, or lateral stress ratio), a measured soil property [84, 42]. By also knowing the void fraction of the soil, ϕ, and the particle and pore fluid density, ρ_p and ρ_f, respectively, p_0 can be determined with

$$p_0 = K_0\sigma'_{v0} + u = K_0 gh(1-\phi)(\rho_p - \rho_f) + \rho_f gh. \tag{3.9}$$

Failure of the substrate will occur when p_i is lowered to a point where the imbalance of two principal effective stresses produces a resolved shear stress that exceeds the shear strength of the soil. This failure shear stress can be created by an imbalance between radial and vertical or radial and hoop stresses. Figure 3-2 shows the stress state of each failure mechanism on a Mohr's circle. From the geometry of the circle and the failure envelope defined by the friction angle φ, the relationship between stresses at failure for either mechanism can be defined as

$$\frac{\sigma'_{rf}}{\sigma'_{vf}} = \frac{\sigma'_{rf}}{\sigma'_{\theta f}} = \frac{1-sin\varphi}{1+sin\varphi} = K_a, \tag{3.10}$$

where subscript f denotes the stresses at failure, prime denotes effective stresses, and K_a is referred to as the coefficient of active failure. A point to make about this failure analysis is that it is also valid for cohesive soils. The one difference is that the failure envelope for a cohesive soil does not pass through 0,0 on a Mohr's circle, as cohesive stresses give soil shear strength even when no compressive stresses are applied. At sufficient depths the failure envelope can be approximated as running through 0,0 for any soil type, as compressive stresses due to gravity will dominate cohesive stresses.

Soil failure due to an imbalance between radial and vertical stresses will occur when the applied radial effective stress equals the radial stress at failure. The radial location of the failure surface in this condition, $R_{f_{rv}}$, can be found by combining Eq. 3.3 for radial stress with Eqs. 3.6, 3.8, and 3.10 and realizing that the vertical effective stress at failure and equilibrium is unchanged.

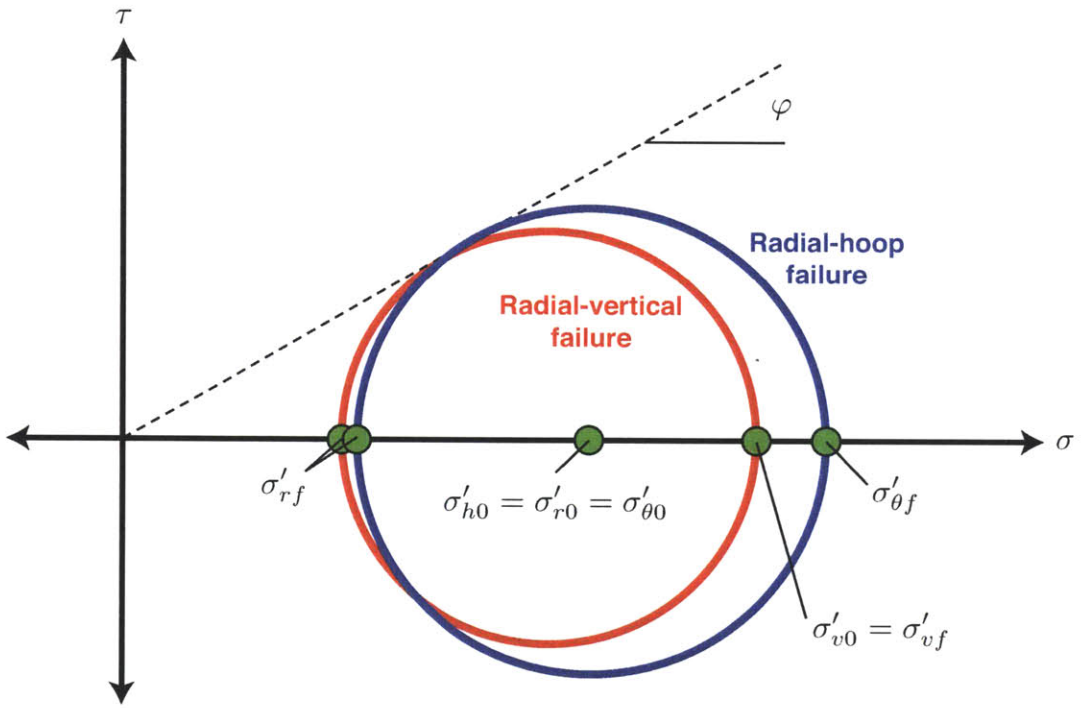

Figure 3-2: Mohr's circle representation of failure in 3D. Local soil failure around a contracting cylindrical body can occur due to either an imbalance of radial and vertical stresses (σ'_{rf} and σ'_{vf} shown by red circle) or radial and hoop stresses (σ'_{rf} and $\sigma'_{\theta f}$ shown by blue circle). The dominant failure mechanism depends on the friction angle and initial stresses in the soil. Lables: σ is normal stress; τ is shear stress; σ'_{h0} is the undisturbed horizontal effective stress; σ'_{v0} is undisturbed vertical effective stress at equilibrium; and φ is the soil's friction angle. Note the radial and hoop stresses are equal in the undisturbed state.

$$\text{failure when: } \sigma'_r = \sigma'_{rf}\big|_{r=R_{f_{rv}}}$$

$$\frac{R_0^2(p_i - p_0)}{r^2} + p_0 - u = K_a\sigma'_{v0} = \frac{K_a}{K_0}(p_0 - u)$$

$$\rightarrow \frac{R_{f_{rv}}}{R_0} = \left[\frac{p_i - p_0}{\left(\frac{K_a}{K_0} - 1\right)(p_0 - u)}\right]^{\frac{1}{2}}. \tag{3.11}$$

If soil failure is caused by an imbalance between radial and hoop stresses, the radial location of the failure surface, $R_{f_{r\theta}}$, can be found by combining Eqs. 3.3 and 3.4 for both stresses with Eqs. 3.6 and 3.10.

$$\text{failure when: } \sigma'_r = \sigma'_{rf}\big|_{r=R_{f_{r\theta}}}$$

$$\frac{R_0^2(p_i - p_0)}{r^2} + p_0 - u = K_a\sigma'_{\theta f} = K_a\left(-\frac{R_0^2(p_i - p_0)}{r^2} + p_0 - u\right)$$

$$\rightarrow \frac{R_{f_{r\theta}}}{R_0} = \left[\frac{(K_a + 1)(p_i - p_0)}{(K_a - 1)(p_0 - u)}\right]^{\frac{1}{2}}. \tag{3.12}$$

The dominant failure mechanism in the soil surrounding a contracting cylindrical body is determined by the type of failure (radial-vertical or radial-hoop) that results in the largest failure surface radius. The ratio of failure radii for both mechanisms can be calculated by combining Eqs. 3.11 and 3.12 into

$$\frac{R_{f_{rv}}}{R_{f_{r\theta}}} = \left[\frac{K_a - 1}{(K_a + 1)\left(\frac{K_a}{K_0} - 1\right)}\right]^{\frac{1}{2}}. \tag{3.13}$$

Figure 3-3 shows Eq. 3.13 plotted for $K_a = 0.19$ to 0.52 and $K_0 = 0.31$ to 1, the maximum range for real soils [84, 42]. Areas greater than one in Fig. 3-3 indicate the failure surface radius is determined by the imbalance between radial and vertical

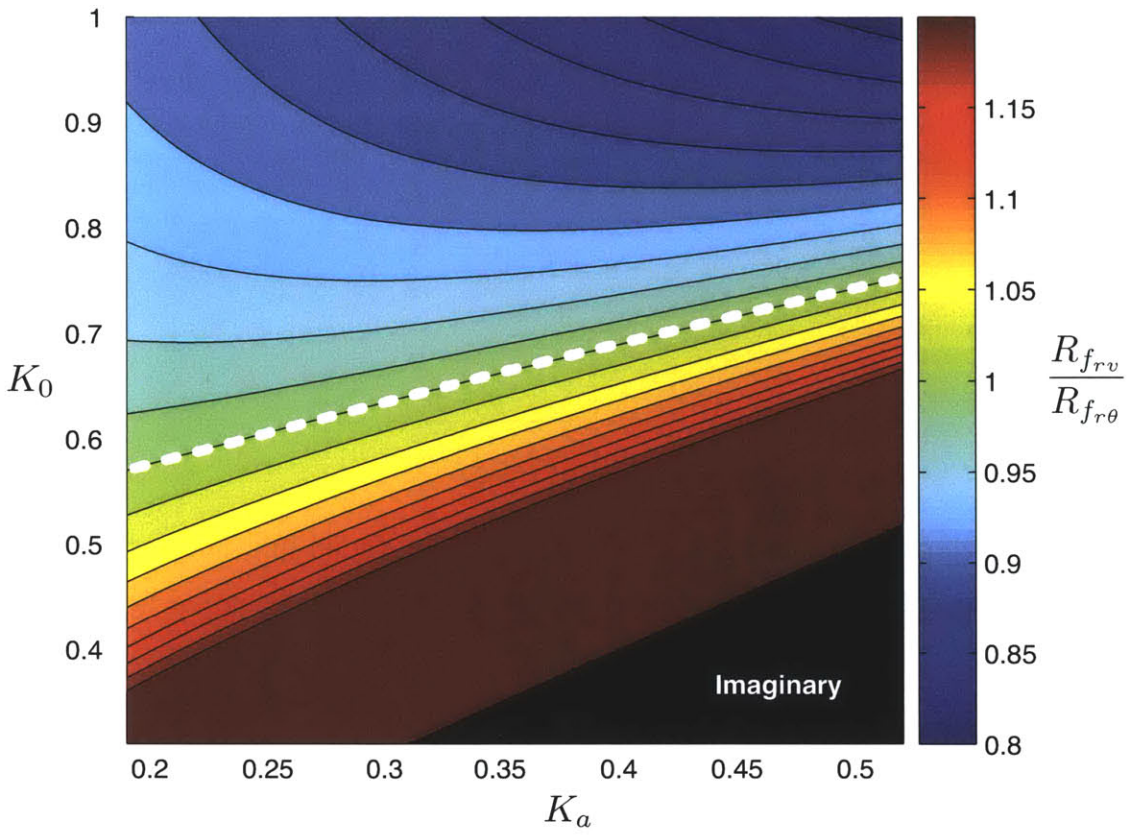

Figure 3-3: Prediction of the dominant soil failure mechanism around a contracting cylinder. Radial-vertical stress induced failure denoted by regions greater than one. Radial-hoop stress induced failure denoted by regions less than one. Dashed white line corresponds to $\frac{R_{f_{rv}}}{R_{f_{r\theta}}} = 1$. Values plotted for the maximum range of K_0 and K_a for real soils.

stresses. Areas less than one indicate the failure surface radius is determined by the imbalance between radial and hoop stresses.

Most values plotted in Fig. 3-3 are on order $\approx$1, indicating that the failure surface radius predicted by both radial-vertical and radial-hoop failure modes will occur at approximately the same location. The only values significantly greater than $\approx$1, reaching order $\approx$10, correspond to radial-vertical failure at low values of K_0. As such, Eq. 3.11 is used to predict the location of the failure surface in the remainder of the thesis.

3.2 Failure surface location predicted by scaling arguments

If during contraction, p_i is assumed to be approximately zero, corresponding to complete stress release between *Ensis'* valves and the surrounding soil, and $\frac{K_0 p_0}{p_0 - u} \approx 1$ because K_0 is often around 0.5 and $u \approx 0.5 p_0$, Eq. 3.11 can be simplified to

$$\frac{R_f}{R_0} \approx (K_0 - K_a)^{-\frac{1}{2}}. \tag{3.14}$$

This expression is depth-independent, does not depend on cohesion, and uses only two parameters commonly measured in a geotechnical survey [2].

Figure 3-4 shows Eq. 3.14 plotted versus the full range of real K_a and K_0 values. Most of the plot lies between values of $1 < \frac{R_f}{R_0} < 4$. These results demonstrate that soil failure around a contracting cylindrical body is a relatively local effect, and for reductions of $p_i \approx 0$, depth-independent.

3.3 Fluidized zone within a failure surface

Ensis' initial valve contraction creates a local cylindrical failure surface in the surrounding soil. As the animal continues to contract its valves, it reduces its own body volume, forcing pore fluid to be pulled into the failure region. Substrate particles within the failure region freely mix with the additional pore fluid, becoming fluidized, while the substrate outside of the region remains static. If the failure radius R_f is known, the change in void fraction within the failure zone can be estimated using

$$\phi_f = \phi_0 + \frac{\Delta V_{Ensis}}{\pi (R_f^2 - R_0^2) L}, \tag{3.15}$$

where ϕ_f is the final (unpacked) void fraction, ϕ_0 is the initial void fraction, and ΔV_{Ensis} is *Ensis'* change in volume during valve contraction.

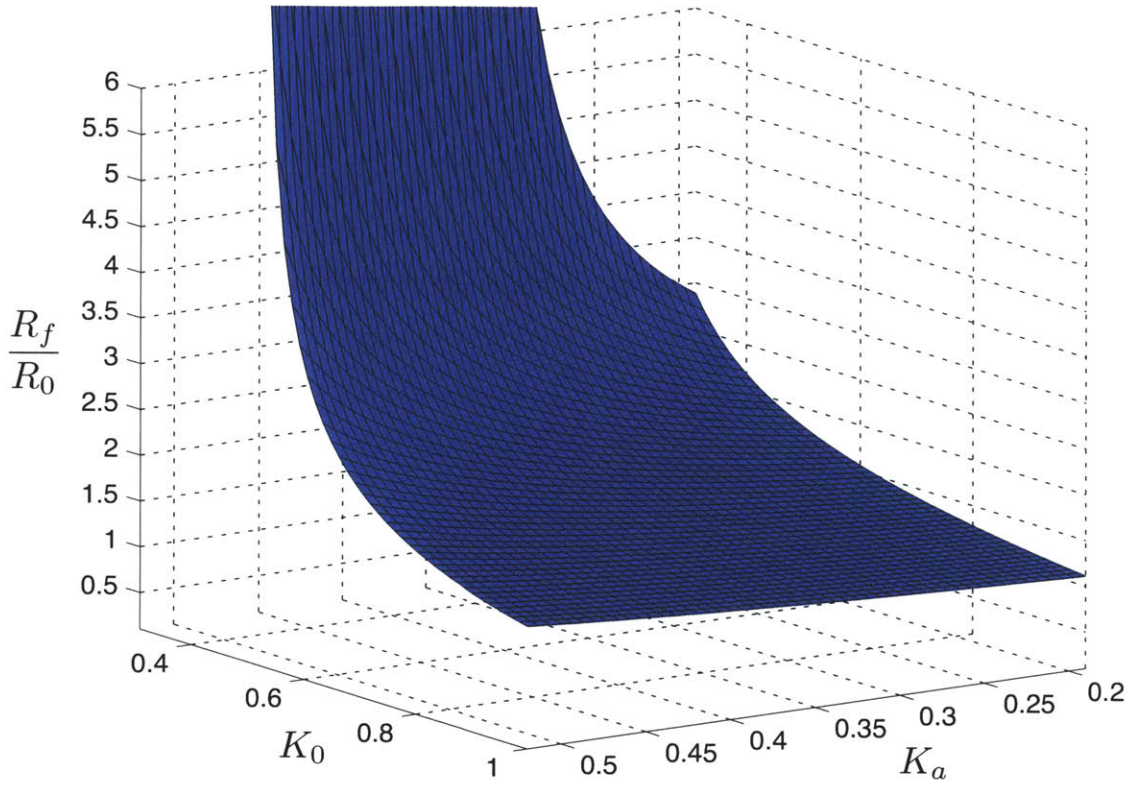

Figure 3-4: Location of soil failure surface around a contracting cylindrical body. Nondimensional location plotted as failure surface radius R_f over initial cylinder radius R_0 using Eq. 3.14. Values of coefficient of lateral earth pressure K_0 and coefficient of active failure K_a reflect the full range found in real soils [84, 42]. The plot shows that soil failure around a contracting cylindrical body is a relatively local effect, occurring at $1 < \frac{R_f}{R_0} < 4$ for most soil types.

3.4 Measurement of localized fluidization in 3D

This section describes the experimental verification of Eq. 3.14. The work presented here was principally conducted by Ludovic Jacob under the direction of Prof. Wolfgang Losert at the University of Maryland[1]. Results and figures in this section were provided by Mr. Jacob, unless otherwise noted.

3.4.1 Mechanical *Ensis* and 3D visualization experimental setup

Soil deformation was measured in 3D by actuating an *Ensis*-inspired mechanism in a mixture of particles and fluid with matched index of refraction. Index-matching creates an optically clear substrate, within which individual particles can be visualized to measure 3D displacements. The mechanism used in these experiments is a manually-operated end effector from RoboClam, the *Ensis*-inspired robot that is explained in detail in the following chapter. The end effector is composed of two "shells" that open and close 6.35mm (0.25in), the same gape displacement as *Ensis'* valves [90]. Figure 3-5 shows the end effector and actuation apparatus used in the 3D visualization experiments.

Figure 3-6 shows the full 3D visualization experimental setup. The end effector was immersed in the granular media at a fixed depth (2 ± 0.5cm between the free surface and the top of the end effector), in the center of a glass container of size 15.5cm $\times$ 15.5cm $\times$ 37.5cm. These dimensions were chosen to minimize wall effects (by maximizing container size) while retaining the ability to image individual particles. Polished borosilicate glass beads (index of refraction $n_p = 1.47$, density $\rho_p = 2230\text{kg} \cdot \text{m}^{-3}$) of 3 ± 0.02mm diameter were used as substrate particles. Index of refraction matched fluid made from dimethyl sulfoxide (DMSO) ($n_{DMSO} = 1.4685$ and $\rho_{DMSO} = 1100.4kg \cdot m^{-3}$) was mixed with the particles. The container was sealed with Argon, as to prevent oxygen contamination of the pore fluid. To tune the index matching, distilled water was added to the DMSO at 4% concentration. A laser dye was carefully

[1]Losert Laboratory - Nonlinear Dynamics of Complex Systems, University of Maryland, IREAP, Paint Branch Drive Bldg 223, Univ. of Maryland, College Park, MD 20742. Email: wlosert@umd.edu. Phone: +1-301-405-6368

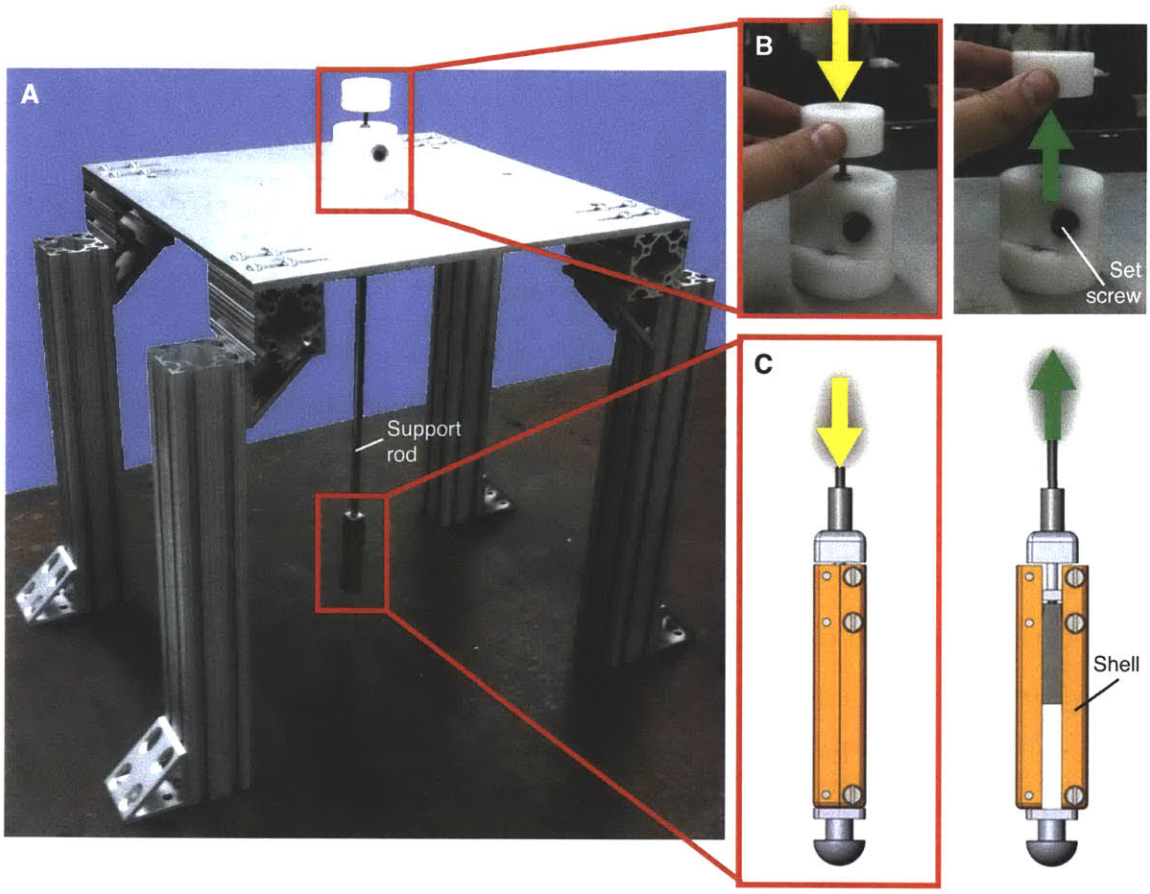

Figure 3-5: *Ensis*-inspired mechanism for 3D substrate deformation measurement. A) Entire device. Zoomed boxes show the actuation plunger and end effector. The platform's legs straddle a container of substrate, in which the end effector is placed. B) Actuation plunger. Set screw in the plunger base tightens a clamp around the support rod to the end effector, which enables its hight to be adjusted. C) End effector. Arrows show corresponding plunger and end effector motions: pushing down on the plunger contracts the end effector shells; pulling up re-expands the mechanism. When in soil, the end effector is covered by a neoprene boot to prevent particles from jamming the mechanism. Details of the end effector design are provided in the following chapter. This figure, as well as the device shown, were made by the author.

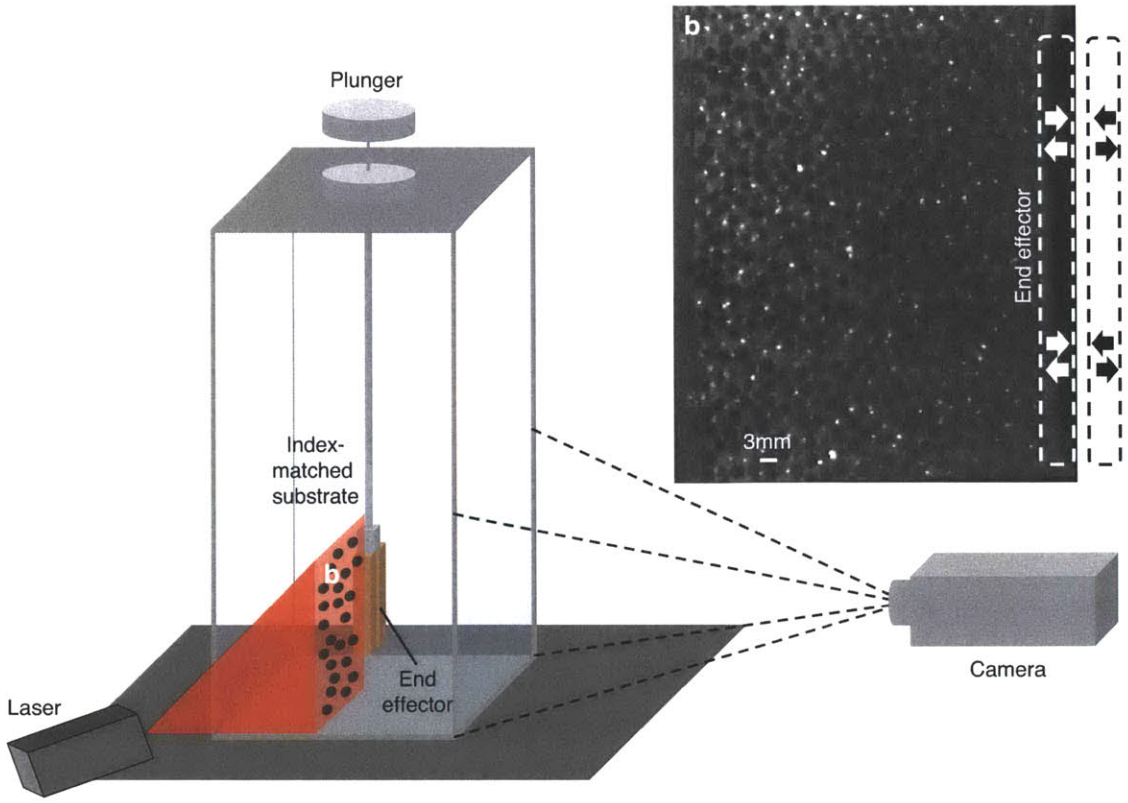

Figure 3-6: 3D substrate visualization experimental setup. The device in Fig. 3-5 is placed over a container of index of refraction matched fluid and substrate, with the end effector in the center of the mixture. A laser sheet illuminates a section of particles in the substrate. Their motion during contraction of the end effector is recorded via a videocamera and measured using PIV. Inset (b) shows a video frame of illuminated particles in a plane orthogonal to one of the end effector shells. Illuminated particles, which are 3mm in diameter, appear as dark spots. One end effector shell can be seen in the right side of the image as a black body. For reference, the location of the entire end effector is shown by dashed lines. Arrows denote motion of the shells.

poured into the mixture as well as hydrochloric acid to avoid photobleaching. As a consequence, beads are seen black and the liquid is white, as shown in Fig. 3-6b.

Experiments were conducted by aligning a laser (50mW) sheet of 659nm wavelength parallel with the support rod and orthogonal to one of the end effector shells, as shown in Fig. 3-6. Particle movements were videotaped with a ProEM 512 high speed videocamera[2], aligned perpendicular to the laser sheet. Behavior of the sub-

[2]ProEM 512 camera. Princeton Instruments, 3660 Quakerbridge Road, Trenton, NJ 08619 USA. `http://www.princetoninstruments.com/Uploads/Princeton/Documents/Datasheets/Princeton_Instruments_ProEM_512B_eXcelon_rev_M2.pdf`. Thanks to E. Fonda and D.P.Lathrop for loaning the camera.

strate around the contracting end effector was imaged at between 50 to 114 frames per second. Particle movement was tracked using the same method outlined in Chap. 1.

3.4.2 3D fluidization experimental results

With an initial void fraction of approximately 38% to 42%, a region of localized fluidization was clearly visualized around the contracting end effector. Variations within this initial void fraction range did not seem to affect the shape of the fluidized zone. Fig. 3-7 shows the ratio between the current and initial void fraction at $0.01s$ after initiating contraction of the end effector. Data are plotted as a function of distance away from the center of the end effector, nondiminsionalized with the end effector's radius. In this image, the end effector shell is situated on the left edge of the figure; the right edge represents the glass wall of the container. Maximum unpacking can be seen to occur within $\frac{r}{R_0} \approx 2$; this result is expected from Eq. 3.14, as the substrate had estimated $K_0 \approx 1$ and $\varphi \approx 25°$, which would yield $\frac{R_f}{R_0} \approx 1.4$. Mottling of the depicted fluidized region is the result of measuring discrete substrate particles. The maximum void fraction in the figure corresponds to $\frac{\phi}{\phi_0} = 1.065$. It is interesting to note that there is a faint appearance of a conical failure surface, denoted by θ_f. Because the end effector is near the top surface of the soil, the formation of a conical failure surface under natural landslide, similar to the 2D wedge-shaped surface in Fig. 2-3D, is expected. This effect is commonly seen at the mouth of ant hills.

Figure 3-8 shows the temporal evolution of the fluidized zone during end effector contraction. This figure was created using data, such as those shown in Fig. 3-7, taken at 0.01s time steps during contraction. The current/initial void fraction ratio was averaged over vertical regions, marked by characteristic lengths away from the center of the end effector. The majority of fluidization occurs within $1 < \frac{r}{R_0} < 2$, which agrees well with the expected failure radius predicted from estimated substrate properties and Eq. 3.14.

Unpacking is also seen within $2 < \frac{r}{R_0} < 4$ in Fig. 3-8, although the substrate was most likely not fluidized within this region. A substrate composed of round spheres

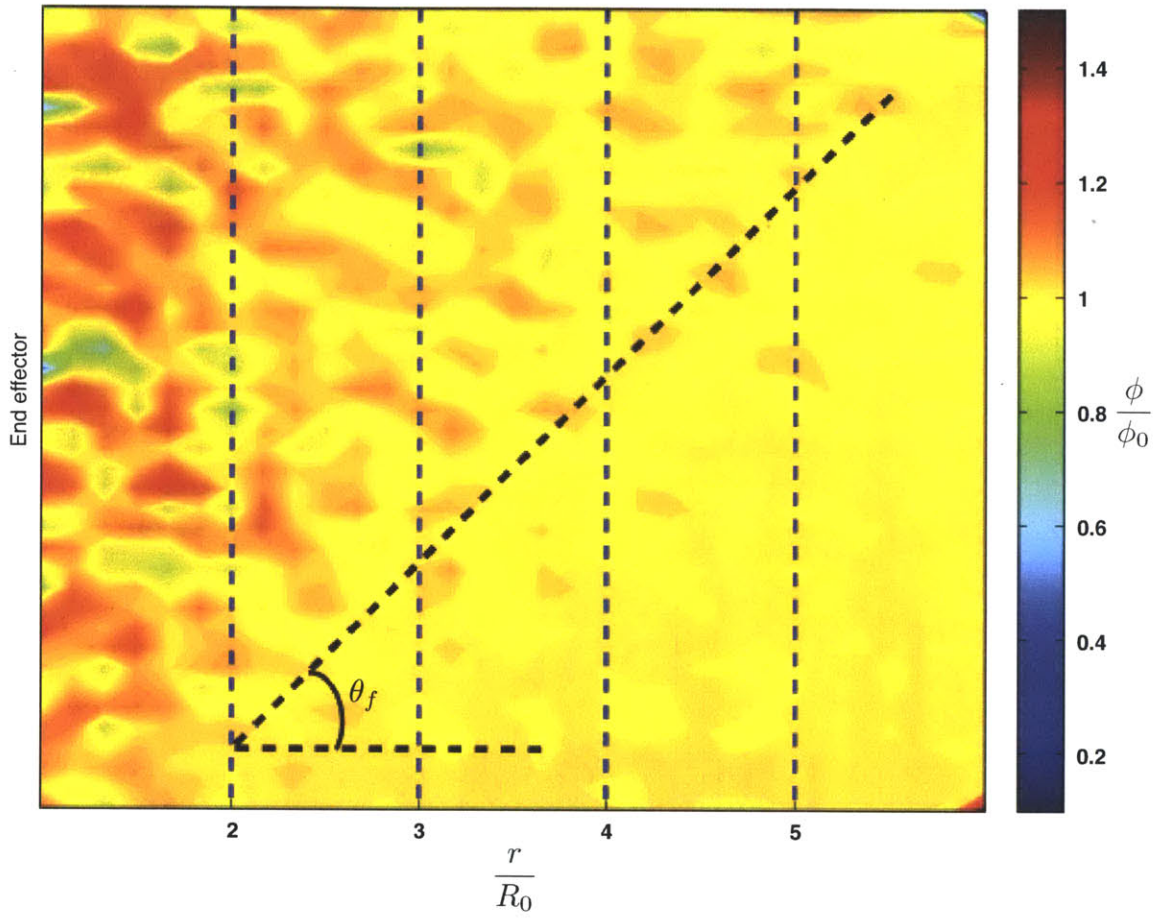

Figure 3-7: Void fraction changes in substrate upon initiation of end effector contraction. Data are plotted as the ratio between current void fraction, ϕ, and initial void fraction, ϕ_0 (which is $\approx 40\%$), as a function of the distance away from the center of the end effector, nondimensionalized with the end effector radius, R_0. These data were taken at 0.01s after initiation of contraction. The plot shows that the most drastic unpacking occurs within $\frac{r}{R_0} \approx 2$, which is within the range expected from Eq. 3.14. The maximum unpacking in the plot is $\frac{\phi}{\phi_0} = 1.065$. Note the faint appearance of a conical failure surface (similar to the mouth of an ant hill), denoted by θ_f. Because the end effector is near the top surface of the substrate, a conical failure surface is expected to form due to natural landslide of the particles, similar to the 2D wedge-shaped surface in Fig. 2-3D.

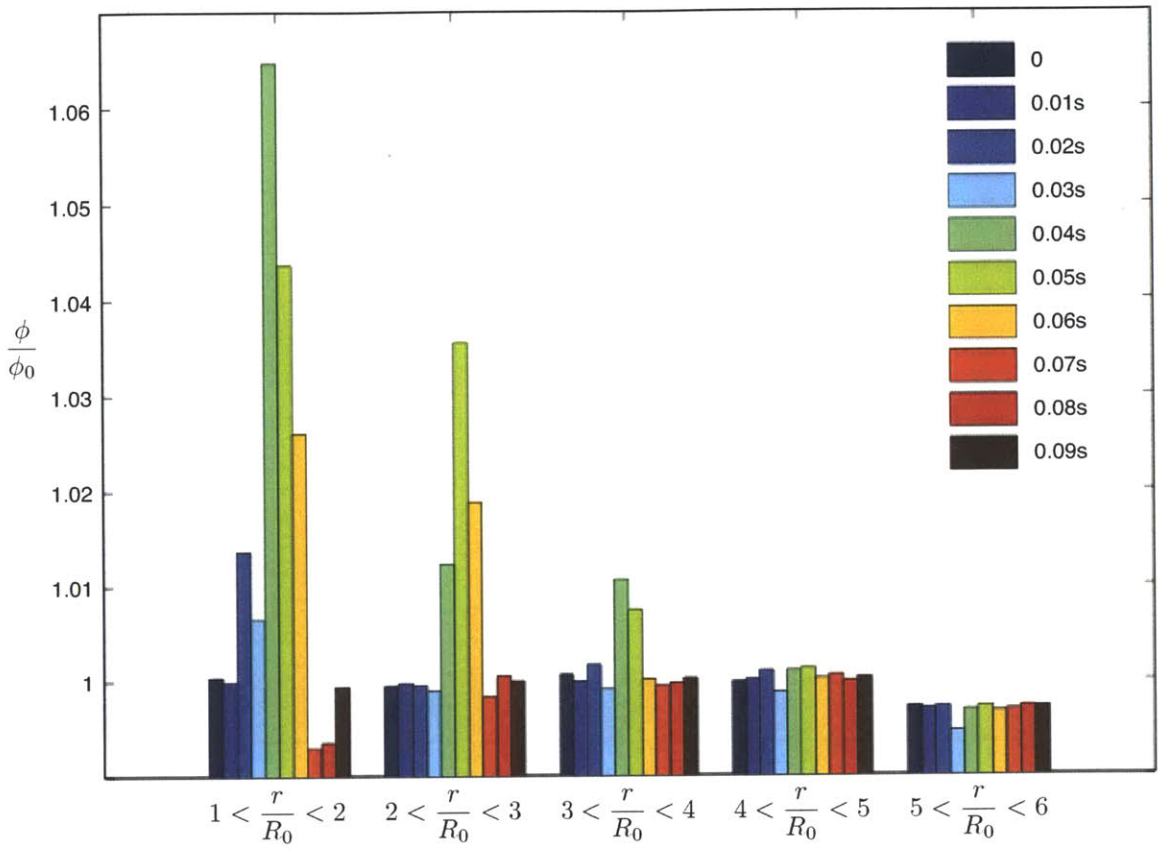

Figure 3-8: Temporal evolution of the fluidized zone. Each cluster of bars represents changes in average void fraction ratio ($\frac{\phi}{\phi_0}$) during contraction of the end effector, with each bar representing a 0.01s step in time. Each cluster is bounded by characteristic lengths away from the center of the end effector. The plot shows that most of the fluidization occurs within $1 < \frac{r}{R_0} < 2$, which agrees well with the expected failure radius from Eq. 3.14. Note that the substrate returns to equilibrium after contraction and fluidization, with $\frac{\phi}{\phi_0} \approx 1$ everywhere. Another interesting effect is the apparent "rebound" within the first region, where the soil overpacks after fluidization before returning to ϕ_0.

should reach incipient fluidization at $\phi \approx 0.41$ [98]. If the particles in this experiment were at an initial void fraction of $0.38 < \phi_0 < 0.40$, incipient fluidization would occur at $1.03 < \frac{\phi}{\phi_0} < 1.08$. As a result, actual fluidization was most likely isolated to the $1 < \frac{r}{R_0} < 2$ region of Fig. 3-8. The unpacking seen in $2 < \frac{r}{R_0} < 4$ is most likely due to the substrate reaching a critical state [102], whereby particles must unpack to freely shear during natural landsliding, indicated by the failure cone in Fig. 3-7.

An interesting effect seen in $1 < \frac{r}{R_0} < 2$ in Fig. 3-8 is the apparent "rebound," where after fluidization the soil enters an overpacked state and then returns to ϕ_0. The cause of this effect is not readily apparent and would be an interesting focus of future research.

Chapter 4

The design and testing of RoboClam: an *Ensis*-inspired robot

Localized fluidization burrowing may have tremendous value in industrial applications. As was shown in Fig. 2-7, moving through a fluidized, rather than static, soil enables *Ensis* to burrow with energy that scales linearly with depth, rather than depth squared. Furthermore, the previous two chapters show that *Ensis* creates localized fluidization using only motions of its valves – a purely kinematic event that does not require additional water to be pumped into the substrate. Due to the animal's simplicity, size scale, and minimal energy consumption, an *Ensis*-inspired burrowing machine should be tractable to design and may offer significant performance advantages over existing technology.

This chapter focuses on the design and testing of RoboClam, an *Ensis*-inspired burrowing robot. The machine was created to validate that localized fluidization can be transferred from biology to technology, and to explore the parametric relationships that govern burrowing performance. RoboClam uses a genetic algorithm, which enables the machine to "evolve" efficient digging kinematics. With localized fluidization, the robot has achieved burrowing performance comparable to the animal in widely different soil types: idealized granular glass beads and *Ensis'* native cohesive mudflat habitat.

4.1 Device scaling

Ensis outputs a peak power of approximately 1.0W during its downward stroke [90], which is dissipated in the surrounding substrate. If the fluidized substrate is responsible for drag, the power required to submerge should scale with size squared and velocity cubed. This assumes high Reynolds number flow – the worst case scenario compared to power dissipated in Stokes flow, which scales linearly with size and with the square of velocity [41].

RoboClam was designed to be tested in real marine substrates, as to avoid wall effects caused by a container, and to capture the peculiarities of real soil with heterogeneous composition and the presence of organic matter. To do this, RoboClam required a power source compatible with marine environments. A standard $80ft^3$ scuba tank pressurized to 3000psi was a logical choice, as it contains approximately one-quarter the energy of a 12V 35Ah lead acid car battery [4, 71]. Energy in a battery is determined by its voltage (V) multiplied by its capacity (Ah). Energy in a scuba tank is determined by its pressure multiplied by its volume.

By knowing the power output of real *Ensis* and the anticipated drag scaling with size and speed, an $80ft^3$ scuba tank was predicted to enable a robotic clam to be sized from 0.5X to 2X the animal, move up to 3X as fast, and run for nearly 1.5h at max size and velocity. Thus, it was decided that RoboClam would be able to accept three digging end effectors, sized 0.5X, 1X, and 2X that of real *Ensis*, based on length.

4.2 End effector mechanism design and frictional analysis

RoboClam uses an *Ensis*-shaped end effector to dig into soil, shown in Fig. 4-1A. The end effector requires two degree-of-freedom motion: up/down and in/out. *Ensis* opens and closes its valves approximately 6.4mm (0.25in) [90]. To test the effect of in/out displacement on burrowing, the end effector was designed to open 2X as far as the animal's valves. This required the 0.5X scale end effector, which is only

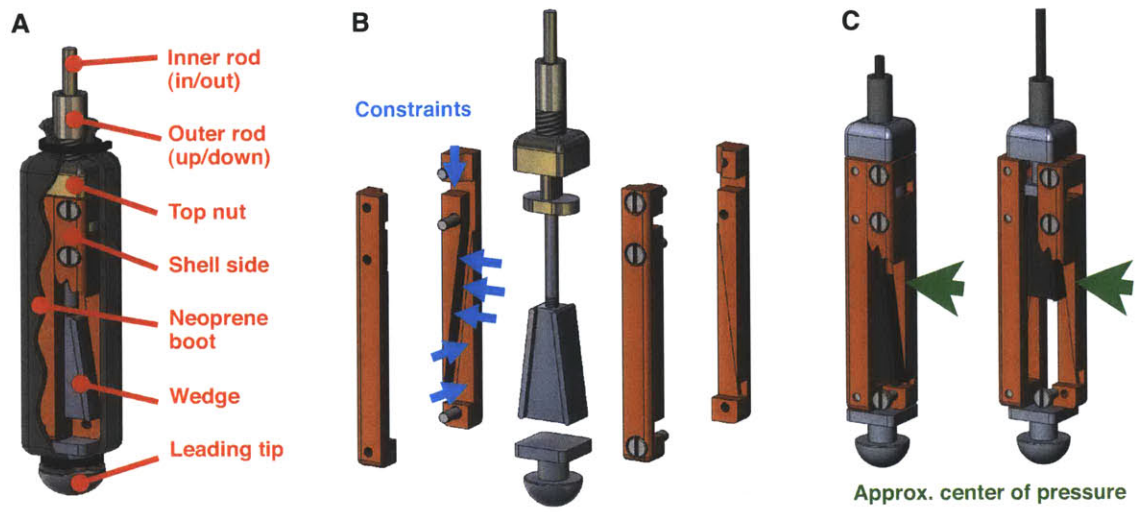

Figure 4-1: RoboClam end effector design. A) End effector packaging. The inner rod connects to the wedge, which slides up and down to force the shell sides in and out. The outer rod attaches to the top nut and moves the entire mechanism up and down. These motions mimic *Ensis'* shell kinematics, as shown in Fig. 1-4. The entire end effector is covered by a neoprene boot to prevent soil particles from jamming the mechanism. The leading tip prevents movement through soil from tearing the boot. B) Exploded view of the end effector mechanism. The mechanism is exactly constrained to prevent jamming and to facilitate the prediction of internal loads, as shown by Fig. 4-2. Six constraints on one shell side, limiting six degrees of freedom, are shown with blue arrows. C) Approximate location of the center of pressure acting on the end effector. The wedge was designed to always straddle the center of pressure to prevent moment loads, and thus high friction, from developing between the wedge and shell sides.

9.97cm long and 1.52cm wide, to open 6.4mm. Displacement of the mechanism is accomplished with a sliding wedge that moves the two shells of the end effector in and out. Figure 4-1B is an exploded view of the mechanism showing how all moving parts are exactly constrained, with contact lengths/widths greater than two to prohibit jamming during any part of the stroke [75]. Furthermore, Fig. 4-1C demonstrates how the wedge was designed to intersect the center of pressure on the shell regardless of its position, assuming the center of pressure is located approximately at the center of the shell. This prevents the shell from exerting moments on the wedge that could increase frictional losses in the mechanism.

The rod used to actuate in/out movement via the sliding wedge is housed within the rod to move the end effector up and down, providing a compact coupling to

RoboClam's actuation and measurement systems. Furthermore, the cross-sectional area of the rod is significantly less than that of the end effector, as to minimize its effect on burrowing drag. The end effector is advanced into soil by the outer rod pushing downwards on the mechanism. Real *Ensis* pulls its valves downwards using a foot – a soft, dexterous organ that would be very difficult to mimic with a machine. Since data presented in the preceding chapters indicates that *Ensis'* valves, and not its foot, are responsible for localized fluidization, RoboClam uses a pushing actuation scheme to allow for all actuators and sensing equipment to be packaged above the soil surface for mechanical simplicity.

The transmission ratio, TR, for the end effector can be derived from the free body diagram in Fig. 4-2 as

$$TR = \frac{H}{F} = \frac{1}{2}\left[\frac{\cos\theta - \mu\sin\theta}{\sin\theta + \mu\cos\theta} - \mu\right], \tag{4.1}$$

where F is the force acting on the wedge from the inner rod, H is the force transferred from the side shell to the soil/neoprene boot, μ is the coefficient of friction between the side shells and wedge/top nut, and θ is the wedge angle. The efficiency of the mechanism can therefore be calculated by computing the work done over a stroke with

$$\eta = \frac{E_{out}}{E_{in}} = 2\frac{H\delta_x}{F\delta_y} = 2TR\sin\theta, \tag{4.2}$$

where E_{in} is mechanical energy put into the mechanism, E_{out} is energy dissipated to the soil, δ_x is the incremental movement of each side shell, and δ_y is an incremental movement of the wedge.

The end effector is made from alloy 932 (SAE 660) bearing bronze[1] and 440C stainless steel[2]. These materials were chosen because both are saltwater compatible and have a low coefficient of sliding friction when lubricated [3]. The dynamic coefficient of friction within the mechanism, when lubricated with silicon oil, was measured

[1]Bearing-Grade Bronze (Alloy 932). McMaster Carr. `http://www.mcmaster.com`
[2]440C stainless steel. McMaster Carr. `http://www.mcmaster.com`

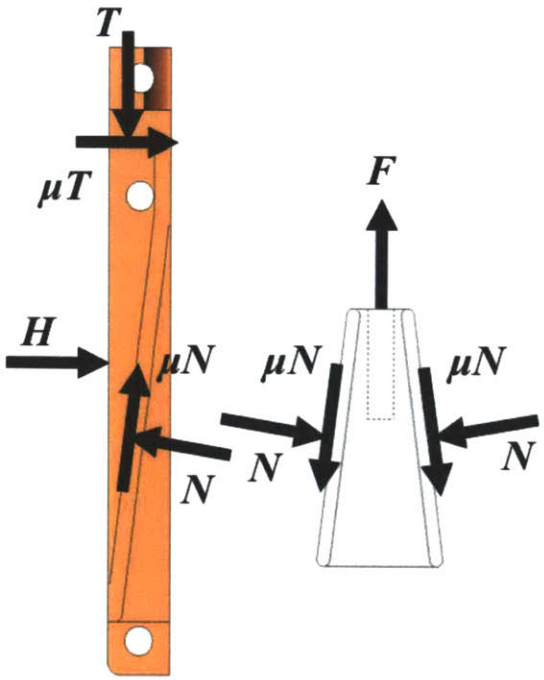

Figure 4-2: Free body diagram of one shell side and the wedge within the end effector. Arrows denote forces. Labels: F is the force acting on the wedge from the inner rod, N is the normal force acting between the wedge and the shell sides, T is the reaction force between the top nut and the shell side, H is the force transferred from the shell side to the soil/neoprene boot, and μ is the coefficient of friction between the shell sides and wedge/top nut.

to be 0.17 with 0.013 standard deviation under horizontal loads ranging from 13.3N to 83.7N. In addition to providing adequate lubrication, silicon oil was used in the end effector because it does not get absorbed by neoprene like petroleum-based oils.

The wedge angle was chosen to be 7.13° in order to maximize contact lengths/widths while enabling the smallest end effector to be 0.5X the size of *Ensis*. Since the TR increases with decreased θ and μ, this geometry yields a relatively high TR of 1.55, with a maximum of 1.83 and minimum of 1.33 corresponding to frictional variations. The resulting efficiency is 39% with a minimum of 33% and a maximum of 46%. This level of efficiency is tolerable; packaging size, jam-free operation, and the ability to calculate lost energy outweighed the need for high efficiency when designing the end effector. If efficiency is critical in future design iterations, a maximum of 60% can be achieved by using a similar design with the same materials and a wedge angle of 29°.

4.3 Robot packaging

The RoboClam actuation system is composed of two nested pneumatic pistons, as shown in Fig. 4-3. The lower piston rod connects to the top of the end effector and controls up/down movement. The upper cylinder controls the in/out motion of the effector mechanism via the in/out rod, which runs through the center of the lower piston rod. The nested piston configuration was chosen because it enables each degree of freedom to be actuated independently and provides a low-profile connection to the end effector.

Pressure is regulated down from the scuba tank (or air supply during lab testing) to four independent regulators, one for each piston inlet. Air pressure delivered to the pistons is measured by a transducer at each input port. Displacements of the lower and upper pistons are measured by a string potentiometer and an integrated linear potentiometer, respectively. Sensor excitation, data acquisition, pressure regulation, and control of the solenoid valves that send air to the pistons are managed by a USB DAQ device[3]. Power to the DAQ is provided by USB, and power to the solenoid

[3]NI USB-6009. National Instruments. `http://www.ni.com/`

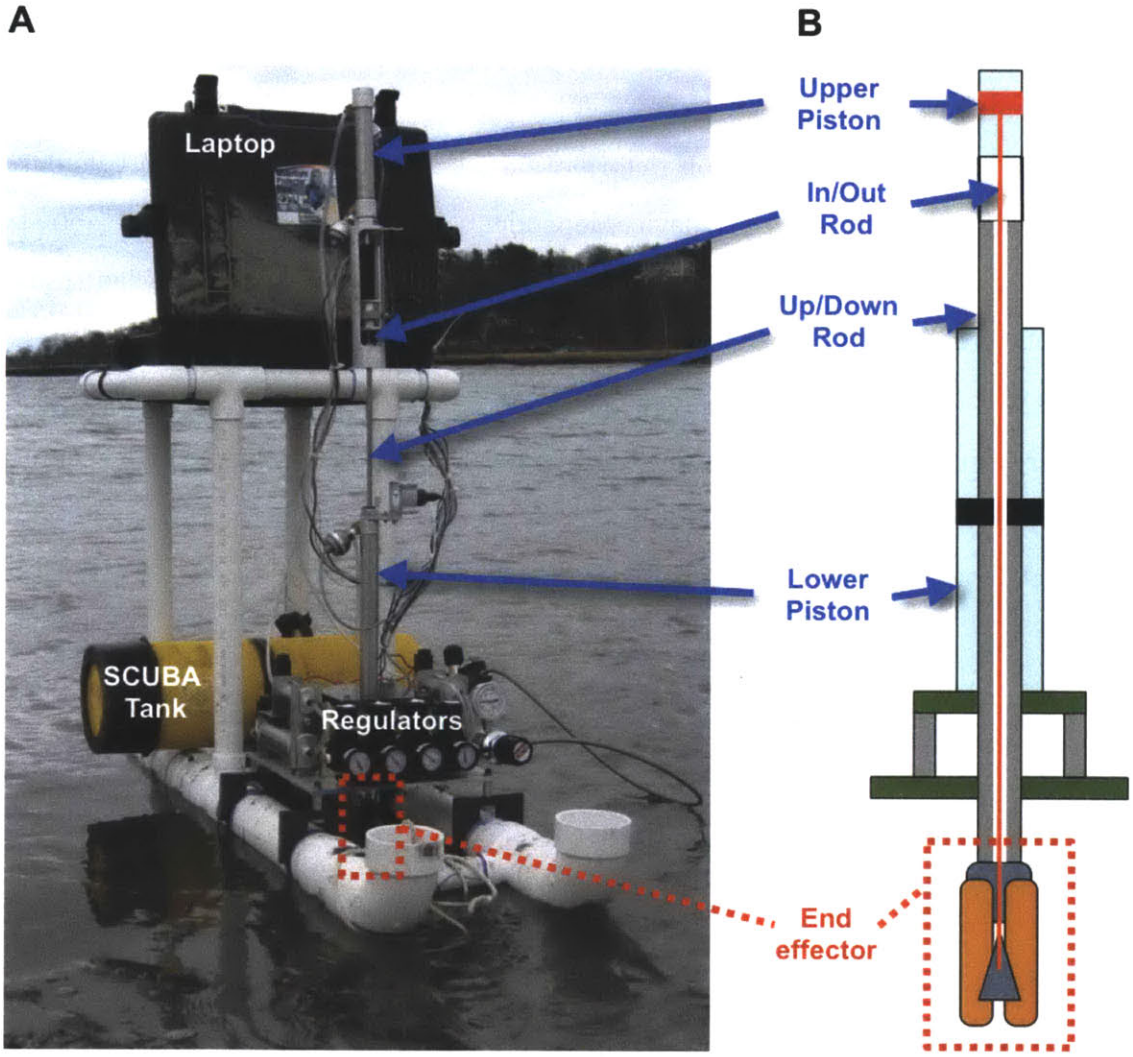

Figure 4-3: Anatomy of the RoboClam robot. A) RoboClam being tested in Gloucester, MA in real *Ensis* habitat. The machine is powered with a SCUBA tank and controlled via an onboard laptop. Pressure regulators regulate the forces for each stroke of the burrowing cycle. B) Schematic of the nested piston actuator architecture. The lower piston moves the end effector up and down via the up/down rod. The upper piston expands and contracts the end effector via the in/out rod, which passes through the center of the up/down rod.

valves is provided by two small, onboard lead acid batteries.

4.4 Burrowing energy expenditure calibration

To determine whether *Ensis*-inspired digging provides an advantage over other methods, the energy expended in soil deformation while burrowing must be calculated. The overall energy consumed is device-dependent; the purpose of creating RoboClam was to test a new burrowing *method* that is more efficient than current methods. After this method is identified, machines used to exploit it can be designed for optimized efficiency.

Energy expended deforming soil while burrowing can be calculated by accounting for input energy minus all of the other losses in the system. For the up/down motion of RoboClam, the energy lost to soil deformation during one stroke is

$$\begin{aligned} E_{soil} &= E_{in} - E_{friction} - E_{potential} \\ &= \int_{\delta_1}^{\delta_2} \Delta p_u A_u dy - |F_{u,friction}(\delta_2 - \delta_1)| - m_u g(\delta_2 - \delta_1), \end{aligned} \tag{4.3}$$

where the subscript u designates the up/down piston, Δp_u is the pressure differential over the piston, δ_1 and δ_2 are the starting and ending displacements of the stroke, A_u is the area of the piston, $F_{u,friction}$ is the measured frictional force in the piston, and m_u is the total mass moving up and down. The energy transferred to the soil during the in/out motion is represented by

$$\begin{aligned} E_{soil} &= \eta(E_{in} - E_{friction} - E_{potential}) - E_{boot} \\ &= \eta \left[\int_{\delta_1}^{\delta_2} \Delta p_i A_i dy - |F_{i,friction}(\delta_2 - \delta_1)| - m_i g(\delta_2 - \delta_1) \right] - 0, \end{aligned} \tag{4.4}$$

where the subscript i represents the in/out piston, δ_1 and δ_2 are the starting and ending displacements of the stroke, η is the efficiency defined in Eq. 4.2, Δp_i is the pressure difference over the piston, A_i is the area of the piston, $F_{i,friction}$ is the measured frictional force in the piston, and m_i is the total mass of the in/out linkage moving up and down. E_{boot} proved to be very difficult to measure. Since this energy results from elastic deflection of boot, it was taken to be zero over a full in/out cycle. This is a conservative assumption, as any energy lost to hysteresis caused by the viscoelasticity of the neoprene will appear as additional energy dissipated in the soil.

4.5 Genetic algorithm design

In testing RoboClam, the sequence of the machine's motions (up stroke, contraction, down stroke, expansion) was never varied. These motions directly mimic *Ensis'* valve kinematics during burrowing, shown in Fig. 1-4. The space of control parameters was reduced to the pneumatic pressure applied and the duration or displacement of each movement. Through experimentation, it was found that time control of the upward and downward motions and displacement control of the inward and outward motions resulted in successful burrowing in marine soils. This yielded eight independently-controllable parameters: upward and downward time, inward and outward displacement, and upward, downward, inward, and outward pressure. In later laboratory tests, in/out motions were also time controlled.

During all tests, the robot's control parameters were controlled by a genetic algorithm (GA)[4]. A GA was chosen because it can handle many independent variables in an optimization problem. The random mutation and recombination of traits used by a GA also tend to allow it to find a global minimum, even in situations in which other optimization methods would not [27]. During early tests, MATLAB's[5] built-in GA

[4]It should be noted that Robin L.H. Diets, who was a member of this project under the MIT Undergraduate Research Opportunities Program, conceived of the idea of using a GA to optimize RoboClam performance. This was an invaluable insight, from which the project greatly benefited, and for which Robin deserves much credit. Robin also developed all of the GA software, first adapting Matlab and then writing a full software package in Python.

[5]Matlab. The Math Works. 3 Apple Hill Drive, Natick, MA 01760-2098. `http://www.mathworks.com/`

was chosen for RoboClam testing, with a population of 10-20 individuals running for 10-20 generations. In later tests, RoboClam ran from customized software written in Python[6].

A Genetic algorithm works like evolution in nature [27]. In the case of RoboClam, the GA begins a test by randomly generating a population of individuals, where each individual is a set of instructions (movement times/displacements and pressures) to run the machine. The GA runs the robot with each individual and records its digging performance. Individuals are then compared by a metric to be optimized – a "cost" function that relates to digging efficiency for RoboClam. Individuals in the population with the lowest cost are allowed to interbreed (mix parameters) with each other, high-cost individuals are killed off, and new individuals are added to the population to form the next generation. The process repeats for many generations, ideally continually decreasing the cost to a global minimum, which appears as a cost asymptote.

In quantifying optimized burrowing efficiency, two factors proved to be relevant: the overall energy expenditure per depth of the robot, β, where $\frac{E}{\delta} = \beta$; and the power law relationship, α, between depth and energy expended, where $\alpha = \frac{\ln E}{\ln \delta}$ with the energy-depth data centered about $(0, 0)$. Two cost functions were used during RoboClam testing. In ocean tests, the cost was

$$cost_{ocean} = \beta\alpha, \tag{4.5}$$

as minimizing β only resulted in low-energy burrowing for depths of 20-30cm, but with relatively high α (≈ 2). At greater depths these burrowing techniques would be useless, as required energy would exponentially increase. As a result, Eq. 4.6 was used for the cost function, with the intent of minimizing α to 1 and β as small as possible. Burrowing with $\alpha = 1$ indicates localized fluidization, such as was shown in Fig. 2-7. In laboratory tests, the cost function used was

$$cost_{lab} = \alpha \tag{4.6}$$

[6]Python Programming Language - Official Website. Python. `http://www.python.org/`

because demonstrating localized fluidization burrowing was the goal the experiments.

4.6 RoboClam performance

Figure 4-4 shows data from the best digging trial obtained during 125 tests in real *Ensis* habitat off the coast of Gloucester, MA. During these tests, the GA varied up and down time, in and out displacement, and the pressures associated with each movement. The cost optimized was the relationship given in Eq. 4.6. As can be seen from the figure, RoboClam achieved nearly depth-independent drag resistance, with an energy versus depth power law slope of $\alpha = 1.17$. To contrast this, *Ensis*-shaped blunt body (Clamcicle) pushing data, measured in the same substrate and also shown in Fig. 2-7, is included in the plot, yielding an expected exponentially higher power law relationship, with a best-fit of $\alpha \approx 2$.

Figure 4-5 shows the best digging trial obtained during RoboClam lab testing in 1mm soda lime glass beads, the same substrate used to test real *Ensis* in the experimental setup in Fig. 2-2. Through hundreds of tests performed over a period of months, it was determined, through both GA results and observation of the machine, that burrowing performance is most sensitive to in and out motions of the end effector. The test shown in Fig. 4-5 involved no active up and down movements, with the robot propelled merely by its own weight. Digging data in this plot demonstrates a perfectly linear relationship between burrowing energy vs depth, indicating depth-independent drag resistance and localized fluidization. The pushing data shown, which exhibits the expected power law relationship of $\alpha \approx 2$, was obtained by pushing the robot into the substrate with steadily increasing force, as shown in inset b.

Surprisingly, the data in Figs. 4-4 and 4-5 show that RoboClam can burrow with localized fluidization in two substrates with vastly different behaviors: one ideally granular (Fig. 4-5) and the other inhomogeneous, cohesive, and with organic content (Fig. 4-4). This can be rationalized with Eq. 3.14 ($\frac{R_f}{R_0} \approx (K_0 - K_a)^{-\frac{1}{2}}$), which does not depend on cohesive stresses or particle size. Both cohesive and granular soils will have values for K_0 and K_a. This result indicates that localized fluidization burrowing

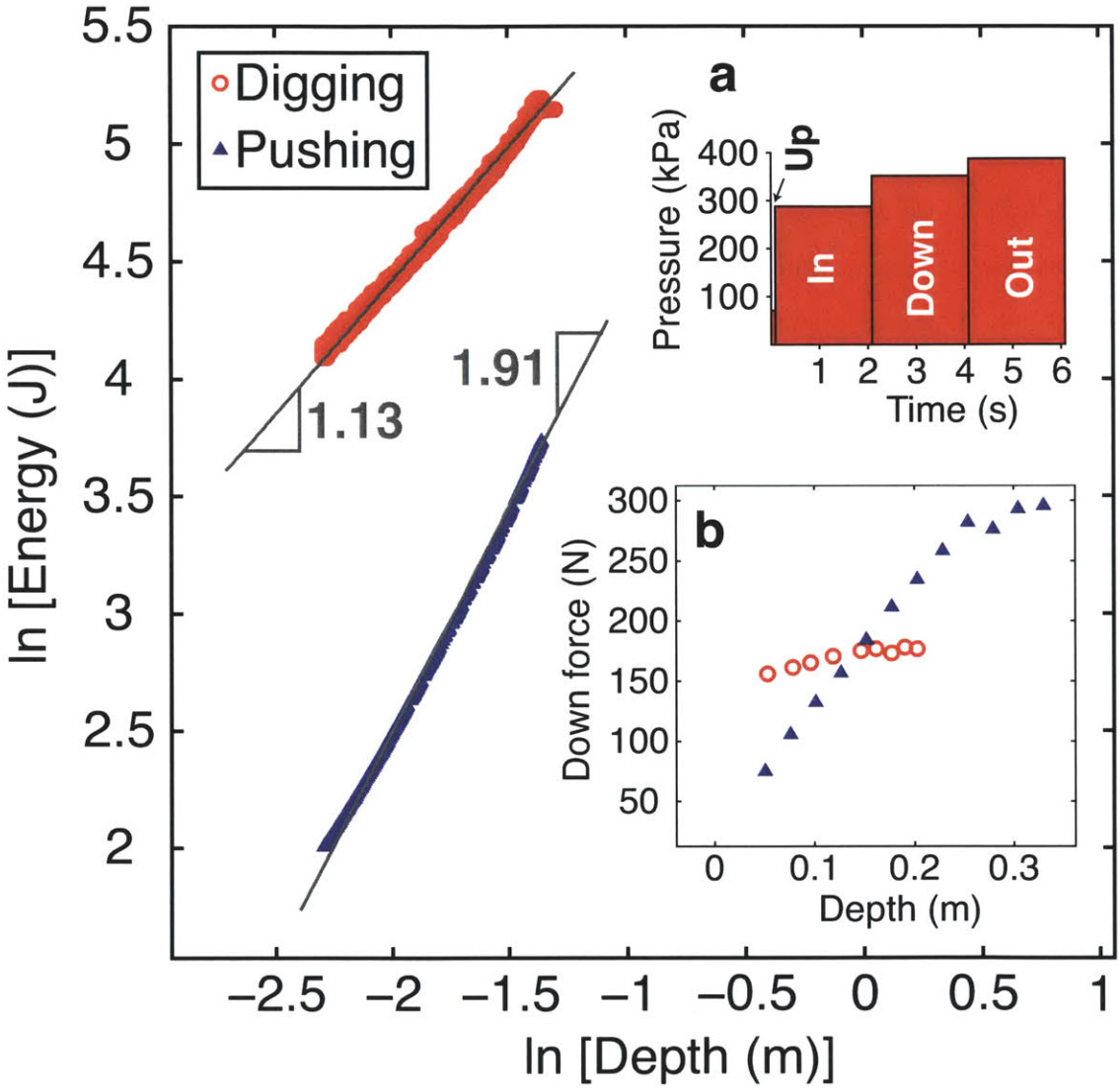

Figure 4-4: RoboClam burrowing data showing energetic advantages of localized fluidization in ocean mudflat soil. Digging data is from the best test, determined by a genetic algorithm, out of 125 gathered in *Ensis* habitat in Gloucester, MA. Pushing data is from the *Ensis*-shaped blunt body (Clamcicle) taken in the same location. The power law exponent of digging is near the ideal of $\alpha = 1$ due to localized fluidization; pushing data is near the expected value of $\alpha = 2$ for moving in static soil. Inset a) shows the burrowing parameters for the test, plotted as piston pressure and movement times. Inset b) shows the increase in required downwards pushing force in static soil, but relatively constant force in fluidized substrate.

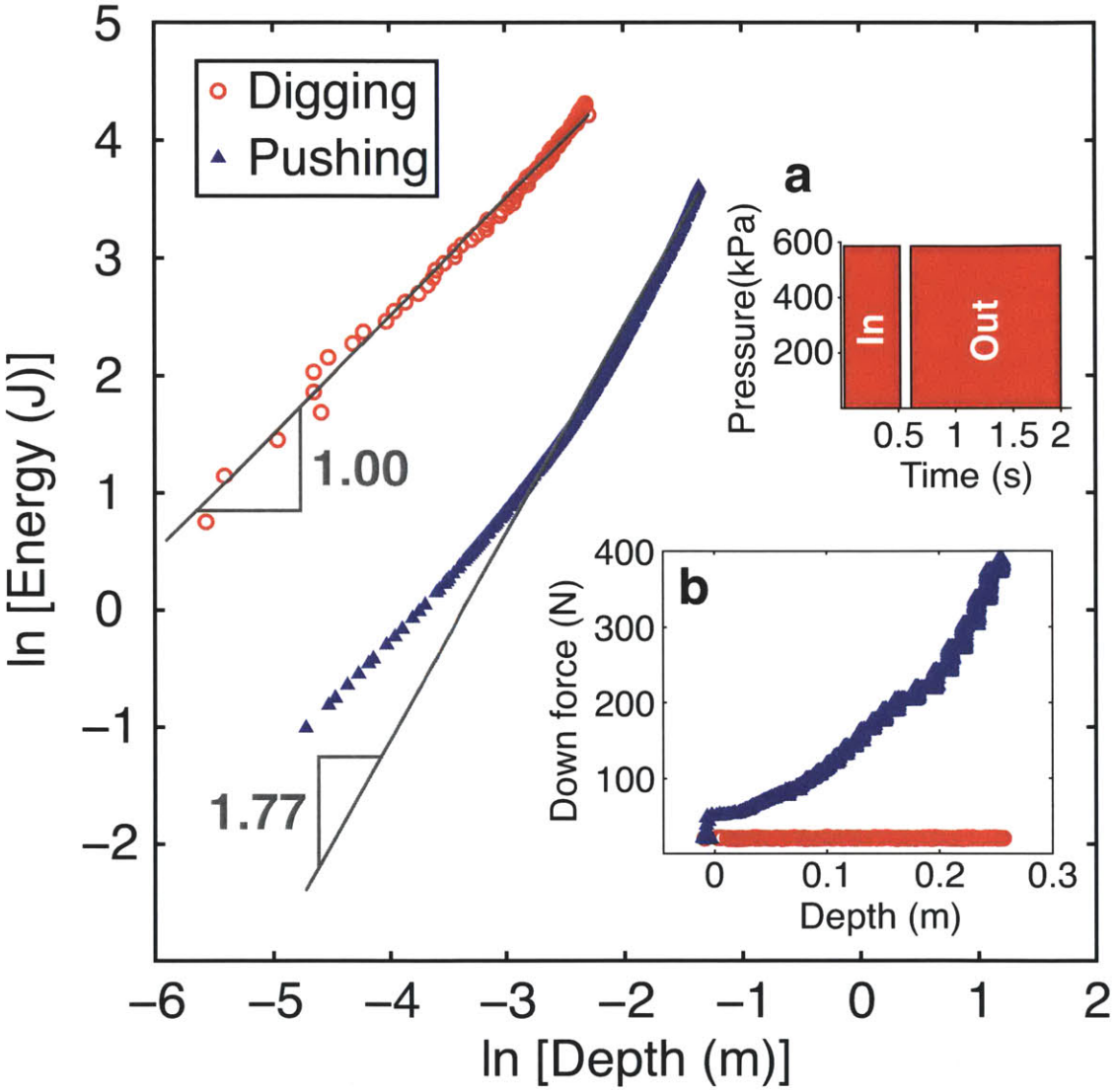

Figure 4-5: RoboClam burrowing data showing energetic advantages of localized fluidization in an idealized granular substrate. Digging data is from the best test, determined from the ideal energy-depth power law relationship of $\alpha = 1$, out of 54 performed in 1mm soda lime glass beads. Pushing data is from the robot slowly submerging into the substrate under increasing down pressure. Contrast between the methods shows *Ensis*-inspired digging achieves depth-independent drag and burrowing energy that scales linearly with depth, rather than $\alpha \approx 2$ for pushing. Only in and out motions of the end effector were actively controlled during digging tests, shown by inset a), with the robot allowed to fall under gravity, shown by inset b).

should be possible in nearly any type of soil. What may change depending on soil type is the source of water used to create a locally-fluidized zone; granular soils allow pore water to flow relatively freely compared to cohesive soils. In the cohesive case, fluidizing water may need to be soured from above, through the burrow left in the wake of the digging machine. Further investigation of local fluidization burrowing in cohesive soils is a rich and interesting area for future research.

Chapter 5

Conclusions and ongoing work

This chapter begins with a summary of the primary contributions presented in this thesis: 1) The discovery of localized fluidization – a novel method of burrowing found in nature; 2) a theoretical derivation and experimental verification of how localized fluidization occurs, taking into account the soil, fluid, and solid mechanics at play; and 3) the design and construction of RoboClam – a robot that burrows via localized fluidization and achieves the same energetic savings as *Ensis*. The remainder of the chapter outlines areas of future research related to localized fluidization burrowing and a proposed path for productizing RoboClam technology.

5.1 Summary of contributions

The following subsections summarize the original research and engineering contributions presented in this thesis.

5.1.1 Discovery of a unique burrowing method in nature

The discovery that *Ensis* uses localized fluidization to reduce burrowing drag and required energy is one of the fundamental contributions of this work. This method of burrowing was previously unknown in nature; its identification constitutes an original scientific contribution to the understanding of animal behavior. Additionally,

localized fluidization burrowing is a novel method of efficiently moving a rigid body through a saturated particulate substrate.

The discovery of localized fluidization burrowing was facilitated by the following research accomplishments. The novel visualization experimental setup shown in Fig. 2-2 enabled *Ensis* to be viewed while burrowing *in situ*. Opaque particles interspersed in the substrate were tracked using particle image velocimetry. These tests showed that the animal uses motions of its shell to create a pocket of fluidized substrate around its body, as depicted by the data in Fig. 2-3. Using theoretical constitutive models for fluidized substrate and experimental results for an *Ensis*-shaped blunt body moving through static soil, it was shown that localized fluidization reduces drag forces to within the animal's strength capability, demonstrated by Fig. 2-6. Additionally, burrowing energy scales linearly with depth when moving through fluidized soil, rather than depth squared in static soil, as shown by Fig. 2-7.

5.1.2 Constitutive understanding of localized fluidization

The second research contribution presented in this thesis is a constitutive understanding of localized fluidization. Fluidization is facilitated by the creation of a cylindrical failure surface in the soil around contracting *Ensis*. The failure surface causes a discontinuity in the soil, allowing particles within to freely fluidize during valve contraction and particles outside to remain static. Using thick-walled pressure vessel equations to describe the stress state in the soil around contracting *Ensis* and soil failure mechanics to predict the stress imbalance to cause failure, expressions for the resulting failure surface geometry were derived.

Simplifying these expressions using governing scaling relationships yielded $\frac{R_f}{R_0} \approx (K_0 - K_a)^{-\frac{1}{2}}$ (Eq. 3.14), a simple expression predicting the failure surface radius given *Ensis'* geometry and two parameters commonly measured in a geotechnical surveys. Applying the full range of geotechnical parameters to this expression showed that the failure surface is a local effect, occurring between one and four characteristic lengths away from the animal for most soil types. This scaling relationship was experimentally verified by testing an *Ensis*-inspired device in a 3D bed of saturated

particles and measuring substrate deformation. These test data, given in Figs. 3-7 and 3-8, show that the failure, and thus fluidized, zone did indeed form within four characteristic lengths from the contracting body.

5.1.3 Localized fluidization burrowing with RoboClam

The third core contribution presented in this thesis is the successful adaptation of localized fluidization burrowing to an engineering system. The RoboClam robot was designed and built to replicate *Ensis'* burrowing kinematics and explore the important engineering and environmental parameters relevant to localized fluidization. Using a genetic algorithm, RoboClam "learned" how dig efficiently by varying digging forces and timescales and tracking burrowing energy expended per depth. The machine successfully matched the animal's performance by achieving a linear energy-depth relationship in both real *Ensis* mudflat habitat and idealized granular substrate, shown in Figs. 4-4 and 4-5. These results are significant, as they demonstrate the viability of localized fluidization burrowing technology for engineering applications in both cohesive and granular soils.

5.2 Topics of ongoing and future investigation

This section outlines future research topics that build upon the work presented in this thesis.

5.2.1 Governing timescales of localized fluidization

Unanswered research questions remain regarding how fast a contracting body (animal or machine) must move to burrow via localized fluidization. If contraction happens too slowly, localized fluidization will not occur and the soil will landslide and fill around the body. The characteristic landslide timescale can be calculated via conservation of momentum applied to a collapsing soil element of arbitrary size, sliding at a failure angle θ_f, as shown in Fig. 5-1A. The net horizontal forces acting on the soil element

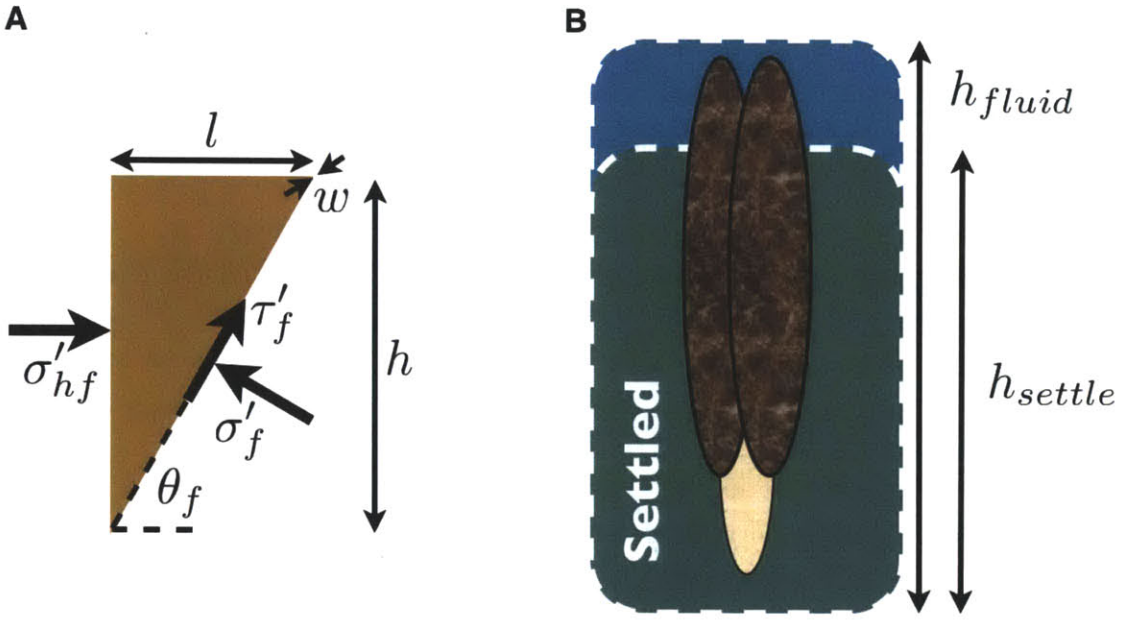

Figure 5-1: Physical effects important to burrowing timescales. A) Stresses and dimensions acting on a soil element during failure. Labels: θ_f is the failure surface angle, σ'_f is normal effective stress acting on the failure surface, τ'_f is shear effective stress acting on the failure surface, σ'_{hf} is horizontal effective stress, and l, w, and h are the arbitrary dimensions of the element. B) Settled substrate around *Ensis* after localized fluidization. Labels: h_{fluid} is the initial height of the fluidized zone and h_{settle} is the height of the particles in the fluidized zone after settling

are $F_h = \int_0^h \sigma'_{hf} w dy$, where w and h are the width and height of the soil element, respectively. Combining this expression with Eqs. 3.6 and 3.9 yields an expression for the acceleration of the soil element, which can in turn be double integrated in terms of time to yield the characteristic time required for the element to slide horizontally along the failure plane one body length l.

$$a_h = \frac{F_h}{m} = \frac{K_a g(1-\phi)(\rho_p - \rho_f)\tan\theta_f}{\rho_p(1-\phi)+\rho_f\phi} \rightarrow t_{char} = \sqrt{\frac{2l}{a_h}}. \tag{5.1}$$

The characteristic time calculated from Eq. 5.1 for 1mm soda lime glass beads saturated in water is 0.3s. Both *Ensis* and RoboClam contract faster, with characteristic times of 0.2s and 0.015 to 0.03s, respectively. Further research lies in inspecting the necessary timescales for contraction to achieve localized fluidization rather than landslide depending on device size and soil type.

The second important timescale in burrowing via localized fluidization is the time available to advance downwards and expand the burrowing body before the fluidized soil settles. Figure 5-1B shows the height of the fluidized zone around *Ensis*, h_{fluid}, and the height of the particles in the zone after settling, h_{settle}. These heights can be correlated through the fluidized void fraction, ϕ_f, and the equilibrium void fraction, ϕ_0, with

$$h_{settle} = \frac{1-\phi_f}{1-\phi_0} h_{fluid}. \tag{5.2}$$

Combining Eq. 5.2 with Richardson and Zaki's equation for settling velocity depending on void fraction, $v_s = v_t \phi^n$ (Eq. 2.7), yields

$$t_{settle} = \frac{h_{fluid} - h_{settle}}{v_s}, \tag{5.3}$$

an expression for the characteristic settling time of the locally fluidized zone around a contracting body.

Using Eq. 5.3 with the change in void fraction shown in Fig. 2-3 and *Ensis'* height as h_{fluid}, t_{settle} = 6.7s. Using *Ensis'* body geometry and change in body volume during contraction reported by Trueman [90] with Eq. 3.14, which predicts the size of the fluidized zone, and Eq. 3.15, which predicts the change in void fraction during fluidization, t_{settle} = 6.0s. Using RoboClam's geometry and kinematics with this same analysis yields t_{settle} = 2.2s. For both animal and machine, respectively, these times are sufficient to advance downwards and complete valve expansion during a burrowing cycle. Future research could expand on this analysis by justifying digging timescales found in nature and predicting the required kinematics of localized fluidization burrowing machines.

5.2.2 Optimization of burrowing kinematics

An interesting optimization problem lies in determining the appropriate digging kinematics of a localized fluidization device given its size and target environment. Eq. 3.15 dictates that the degree of substrate fluidization is linearly proportional to the

volumetric change of the burrowing device during its contraction motion. As soil becomes more fluidized, the effective viscosity will decrease, given by Eqs. 2.14-2.17, and thus the drag force on the burrowing body will also decrease for a given downwards velocity, predicted by Eq. 2.24. But as fluidization increases, so does the settling velocity of the fluidized particles, given by Eq. 2.7. Thus, as fluidization increases, the burrowing device will have to move faster to complete its motions before the substrate settles and will therefore experience increased drag forces. Determining the optimum burrowing kinematics to minimize required power and energy consumption would be tremendously valuable for the design of localized fluidization burrowing devices.

5.2.3 Performance mismatch between *Ensis* and RoboClam energetics

Although RoboClam was able to achieve the same burrowing energy per depth power law relationship as *Ensis*, shown in Figs. 4-4 and 4-5, the overall energy expended per depth was approximately 10X larger for the machine than for the animal, even though the burrowing bodies of both were approximately the same size[1]. Figure 5-2A shows the energy expended per depth on a linear scale for the lowest cost trial of RoboClam ocean testing, with a slope of 2.3J/cm; in contrast, *Ensis'* burrowing energy, predicted from energetics and kinematics associated with the motions in Fig. 1-4, is 0.21J/cm.

The likely explanation for this mismatch is differences in inertia. RoboClam's mass that moves up and down is $\approx$ 2.5kg, whereas *Ensis'* mass is $\approx$ 0.17kg. This means that RoboClam's moving mass will have an order of magnitude higher kinetic energy than *Ensis'* when both dig at the same timescales. This energy must be dissipated in soil deformation at the culmination of each downwards stroke. Figure 5-2B adds credibility to this argument, as it shows RoboClam dug with nearly the same velocity as *Ensis* (0.8cm/s versus 1cm/s) during its lowest cost ocean test.

Further research into the energetic mismatch between *Ensis* and RoboClam will

[1]Frontal area was approximately the same, although RoboClam's end effector length was approximately half that of *Ensis*.

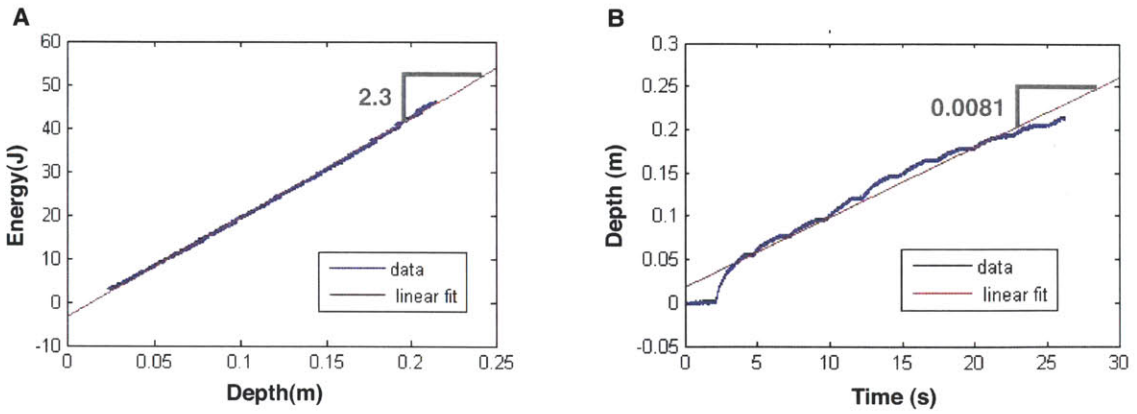

Figure 5-2: RoboClam burrowing data from lowest cost test in *Ensis* habitat. A) Burrowing energy versus depth. B) Burrowing depth versus time.

enable efficient localized fluidization burrowing systems to be designed in the future.

5.2.4 Extracting design rules from RoboClam data

Further research on the topics outlined in the preceding subsections will lead to an understanding of how environmental parameters affect local fluidization burrowing device performance. This understanding will facilitate the formation of design rules that enable engineers to leverage localized fluidization burrowing technology for their specific applications. For example, the design rules will predict required power and on-board energy as a function of device size, substrate type, application depth, and burrowing velocity.

5.2.5 Extension of localized fluidization into dry burrowing applications

Applications such as land mine neutralization, bunker reconnaissance, spacecraft geological surveys, and post-earthquake search and rescue could benefit from compact, lightweight, low-power localized fluidization burrowing devices that can operate in dry substrates. Interesting questions lie in this area, such as how fluidization timescales are affected when the pore fluid is air, with 1000X lower density and 50X lower viscosity than water, and whether there is a kinematic convergence between localized

fluidization and vibratory burrowing systems [50]. This problem presents further biomimetic opportunities to investigate animals that "swim" through dry soil, such as the sandfish lizzard (*S. scincus*) [47].

5.3 Proposed path to productization of localized fluidization technology

The research outlined in the previous section will result in design rules that articulate the parametric relationships that govern the performance of localized fluidization burrowing devices. The first step in commercializing this technology will be to use the design rules to outline the dimensions, application substrate, and anticipated performance of a prototype that will serve as the proof-of-concept for a device that can be commercialized. This design process will entail choosing actuators and energy sources that can meet the timescale and power requirements for achieving localized fluidization and that can be packaged within the device.

Figure 5-3 is a proposed embodiment for a simple, self-contained localized fluidization burrowing device. As the research presented in this thesis indicates that the crux of *Ensis'* burrowing performance is attributed to the animal's valve, and not foot, motions, this first embodiment is modeled after two sets of valves that can contract and move longitudinally relative to each other using the valve kinematics shown in Fig. 1-4 [101]. This embodiment is mechanically simple, does not necessitate a complex mechanism like *Ensis'* foot, and could locomote both up and down in saturated soil.

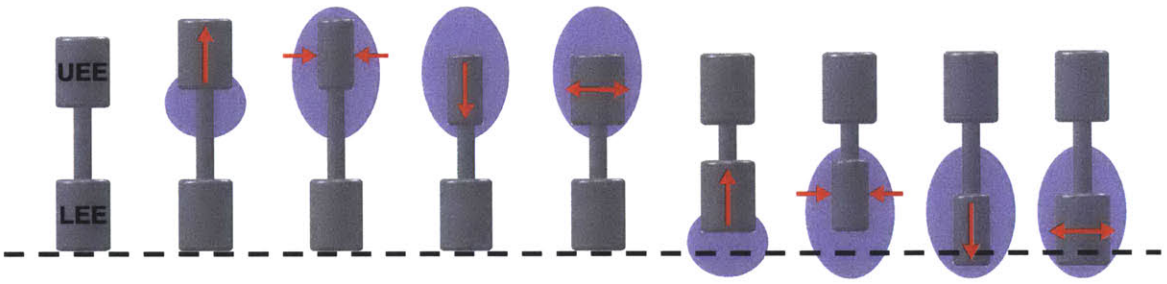

Figure 5-3: Proposed first embodiment of a self-contained localized fluidization burrowing system. The device is composed of an upper end effector (UEE) and lower end effector (LEE) that can each radially contract and move axially relative to each other. Digging progress is achieved by uplifting, contracting, advancing, and expanding the upper end effector and then doing the same progression of motions with the lower end effector, as denoted with red arrows. These motions mimc *Ensis'* valve kinematics, depicted in Fig. 1-4, creating areas of localized fluidization around each end effector, shown by the blue shaded regions.

Bibliography

[1] J. Aoyama, A. Shinoda, S. Sasai, M.J. Miller, and K. Tsukamoto. First observations of the burrows of Anguilla japonica. *Journal of Fish Biology*, 67(6):1534–1543, 2005.

[2] ASTM Standard D4767, 2003, DOI: 10.1520/D4767-04 . Standard Test Method for Consolidated Undrained Triaxial Compression Test for Cohesive Soils. http://www.astm.org/Standards/D4767.htm, 2003.

[3] E.A. Avallone, T. Baumeister, and A.M. Sadegh. *Marks' standard handbook for mechanical engineers*. McGraw-Hill New York etc., 1987.

[4] BatteryMart.com. 12V 35Ah Sealed Lead Acid Battery Insert Terminals. `http://www.batterymart.com/p-12v-35ah-sealed-lead-acid-battery-insert-terminal.html`, 2009.

[5] Bluefin Robotics. 21 inch BPAUV Autonomous Underwater Vehicle. `http://www.bluefinrobotics.com/`, August 2010.

[6] Boston Dynamics. Bigdog - the most advanced rough-terrain robot on earth. `http://www.bostondynamics.com/robot_bigdog.html`, 2009.

[7] R.L. Carroll. Lungfish burrows from the Michigan coal basin. *Science*, 148:963–964, 1965.

[8] B.K.K. Chan, K.K.Y. Chan, and P.C.M. Leung. Burrow architecture of the ghost crab Ocypode ceratophthalma on a sandy shore in Hong Kong. *Hydrobiologia*, 560(1):43–49, 2006.

[9] Chance Anchors. Chance Helical Tieback Anchors. `http://www.abchance.com/resources/technical/31-0502.pdf`, 2008.

[10] Chevron. Chevron Deploys a Second Ultra-Deepwater Drillship. `http://www.chevron.com/news/press/release/?id=2010-03-11`, March 2010.

[11] R.E. Coker. A Perpetual Submarine War. *The Scientific Monthly*, 14:345–351, 1922.

[12] K.J. Coyne, X.X. Qin, and J.H. Waite. Extensible collagen in mussel byssus: a natural block copolymer. *Science*, 277(5333):1830, 1997.

[13] K.M. Dorgan, P.A. Jumars, B. Johnson, BP Boudreau, and E. Landis. Burrowing mechanics: Burrow extension by crack propagation. *Nature*, 433(7025):475, 2005.

[14] J.M. Dormon, C. Coish, C. Cottrell, D.G. Allen, and J.K. Spelt. Modes of byssal failure in forced detachment of zebra mussels. *Journal of Environmental Engineering*, 123:933, 1997.

[15] G.A. Drew. Locomotion in Solenomya and its relatives. *Anat. Anz*, 17:257–266, 1900.

[16] H. Eilers. The viscosity of emulsion of high viscosity materials as function of concentration. *Kolloid, Z.*, 97:313, 1941.

[17] A. Einstein. A new determination of molecular dimensions. *Annalen der Physik*, 19(2):289–306, 1906.

[18] J.R. Ellis and S.E. Shackley. The reproductive biology of Scyliorhinus canicula in the Bristol Channel, UK. *Journal of Fish Biology*, 51(2):361–372, 1997.

[19] Energizer Battery Company. Energizer E91 AA Battery Product Datasheet. `http://data.energizer.com/PDFs/E91.pdf`, 2009.

[20] J.W. Evans. Growth rate of the rock-boring clam Penitella penita (Conrad 1837) in relation to hardness of rock and other factors. *Ecology*, 49(4):619–628, 1968.

[21] E.W. Fager. Marine sediments: effects of a tube-building polychaete. *Science*, 143(3604):356, 1964.

[22] F. Ferrini, D. Ercolani, B. de Cindio, L. Nicodemo, L. Nicolais, and S. Ranaudo. Shear viscosity of settling suspensions. *Rheologica Acta*, 18(2):289–296, 1979.

[23] N.A. Frankel and A. Acrivos. On the viscosity of a concentrated suspension of solid spheres. *Chemical Engineering Science*, 22(6):847–853, 1967.

[24] A. Gaisner. Parental care and reproductive behavior of the clown goby, Microgobius gulosus, with observations on predator interactions. *Environmental Biology of Fishes*, 73(4):341–356, 2005.

[25] L.G. Gibilaro. *Fluidization-dynamics.* Butterworth-Heinemann Oxford, UK, 2001.

[26] P.T. Green. Burrow dynamics of the red land crab Gecarcoidea natalis (Brachyura, Gecarcinidae) in rain forest on Christmas Island (Indian Ocean). *Journal of Crustacean Biology*, 24(2):340–349, 2004.

[27] R.L. Haupt and S.E. Haupt. *Practical genetic algorithms.* Wiley-Interscience, 2004.

[28] R.C. Hibbeler. *Mechanics of Materials.* Prentice Hall, 4th edition, 2000.

[29] E.R. Hinz. *The Complete Book of Anchoring and Mooring.* Cornell Maritime Press, rev. 2d edition, 2001.

[30] A.F. Holland and J.M. Dean. The biology of the stout razor clamTagelus plebeius: I. Animal-sediment relationships, feeding mechanism, and community biology. *Chesapeake Science*, 18(1):58–66, 1977.

[31] E. Holsting. 22-ton oil rig anchor. `http://www.menkent.dk/assistpics/22ton2.jpg`, August 2010.

[32] Hubbell Power Systems. Helical Anchors and Piles. `http://www.abchance.com`, 2010.

[33] A.C. Hurley. Larval settling behaviour of the acorn barnacle (Balanus pacificus Pilsbry) and its relation to distribution. *The Journal of Animal Ecology*, 42(3):599–609, 1973.

[34] L. Ingalls. Burr. flickr creative commons. `http://www.flickr.com/photos/plutor/2525663875/`, May 2008.

[35] H.D. Jones and E.R. Trueman. Locomotion of the limpet, Patella vulgata L. *Journal of Experimental Biology*, 52(1):201, 1970.

[36] S. Jung. Caenorhabditis elegans swimming in a saturated particulate system. *Physics of Fluids*, 22:031903, 2010.

[37] P. Kamermans, H.W. Van der Veer, J.I.J. Witte, and E.J. Adriaans. Morphological differences in Macoma balthica (Bivalvia, Tellinacea) from a Dutch and three southeastern United States estuaries. *Journal of Sea Research*, 41(3):213–224, 1999.

[38] A.R. Khan and J.F. Richardson. Fluid-particle interactions and flow characteristics of fluidized beds and settling suspensions of spherical particles. *Chemical Engineering Communications*, 78(1):111–130, 1989.

[39] M.A.R. Koehl and M.G. Hadfield. Soluble settlement cue in slowly moving water within coral reefs induces larval adhesion to surfaces. *Journal of Marine Systems*, 49(1-4):75–88, 2004.

[40] I.M. Krieger and T.J. Dougherty. A mechanism for non-Newtonian flow in suspensions of rigid spheres. *Journal of Rheology*, 3:137–152, 1959.

[41] P.K. Kundu and I.M. Cohen. *Fluid Mechanics.* Elsevier Academic Press, 2004.

[42] T.W. Lambe and R.V. Whitman. *Soil mechanics.* John Wiley & Sons Inc, 1969.

[43] C.E. Lane. Recent Biological Studies on Teredo–A Marine Wood-Boring Mollusc. *The Scientific Monthly*, 80:286–292, 1955.

[44] F.E. Lloyd. On Pholadidea Penita and its Method of Boring. *Science*, 4(85):188, 1896.

[45] W. Macnae and M. Kalk. The fauna and flora of sand flats at Inhaca Island, Mocambique. *The Journal of Animal Ecology*, 31(1):93–128, 1962.

[46] T.S. Majmudar and R.P. Behringer. Contact force measurements and stress-induced anisotropy in granular materials. *Nature*, 435(7045):1079–1082, 2005.

[47] R.D. Maladen, Y. Ding, C. Li, and D.I. Goldman. Undulatory swimming in sand: Subsurface locomotion of the sandfish lizard. *Science*, 325(5938):314, 2009.

[48] K.H. Mann. Seaweeds: their productivity and strategy for growth. *SCIENCE, VOL 182, NO 4116, P 975-981, DECEMBER 7, 1973. 5 FIG, 2 TAB, 57 REF.*, 1973.

[49] S.H. Maron and P.E. Pierce. Application of Ree-Eyring generalized flow theory to suspensions of spherical particles. *Journal of colloid science*, 11(1):80–95, 1956.

[50] M.E. McCormick. *Anchoring systems.* Pergamon Press, Oxford; New York, 1979.

[51] C. Miller. The Boring Habits of the Shipworm. *The Scientific Monthly*, 19:433–440, 1924.

[52] R.C. Miller and L.C. Boynton. Digestion of Wood by the Shipworm. *Science (New York, NY)*, 63(1638):524, 1926.

[53] N.B. Nair and A.D. Ansell. The mechanism of boring in Zirphaea crispata (L.)(Bivalvia: Pholadidae). *Proceedings of the Royal Society of London. Series B. Biological Sciences*, 170(1019):155, 1968.

[54] O.C. Niederer. Embedding Cablelike Members, 1972. US Patent 3,638,439.

[55] J.A. Nott and B.A. Foster. On the structure of the antennular attachment organ of the cypris larva of Balanus balanoides (L.). *Philosophical Transactions of the Royal Society of London. B, Biological Sciences*, 256(803):115, 1969.

[56] Ocean Specialists Inc. Personal conversations. `http://www.oceanspecialists.com/`, April 2009.

[57] `offshore-technology.com`. Liuhua 11-1, South China Sea, China. `http://www.offshore-technology.com/projects/amoco/images/amo1.jpg`, August 2010.

[58] B. Olesen and K.A.J. Sand-Jensen. Demography of Shallow Eelgrass (Zostera Marina) Populations–Shoot Dynamics and Biomass Development. *Journal of Ecology*, 82(2):379–390, 1994.

[59] G.H. Parker. Locomotion of Sea-Anemones. *Proceedings of the National Academy of Sciences of the United States of America*, 2(8):449, 1916.

[60] G.H. Parker. The behavior of sea-anemones. *Proceedings of the National Academy of Sciences of the United States of America*, 2(8):450, 1916.

[61] L.S. Peck, A.D. Ansell, K.E. Webb, L. Hepburn, and M. Burrows. Movements and burrowing activity in the Antarctic bivalve molluscs Laternula elliptica and Yoldia eightsi. *Polar Biology*, 27(6):357–367, 2004.

[62] M. Phenix. Fish-Inspired Car. *Popular Science*, `http://www.popsci.com/aerodynamic/article/2005-08/fish-inspired-car`, 2005.

[63] E.H. Pinn, C.A. Richardson, R.C. Thompson, and S.J. Hawkins. Burrow morphology, biometry, age and growth of piddocks (Mollusca: Bivalvia: Pholadidae) on the south coast of England. *Marine Biology*, 147(4):943–953, 2005.

[64] J.F. Richardson and W.N. Zaki. Sedimentation and fluidisation: Part I. *Chemical Engineering Research and Design*, 32(a):35–53, 1954.

[65] H.U. Riisgård and P.S. Larsen. Water pumping and analysis of flow in burrowing zoobenthos: an overview. *Aquatic Ecology*, 39(2):237–258, 2005.

[66] P.K. Robertson and R.G. Campanella. Interpretation of cone penetration tests. Part I: Sand. *Canadian Geotechnical Journal*, 20(4):718–733, 1983.

[67] Rocna. Rocna Drag Anchor. `http://www.rocna.com/`, 2010.

[68] R. Rosenberg and K. Ringdahl. Quantification of biogenic 3-D structures in marine sediments. *Journal of Experimental Marine Biology and Ecology*, 326(1):67–76, 2005.

[69] N.L. Ruocco, L.O. Lucifora, J.M. Diaz de Astarloa, and O. Wohler. Reproductive biology and abundance of the white-dotted skate, Bathyraja albomaculata, in the Southwest Atlantic. *ICES Journal of Marine Science*, 63(1):105, 2006.

[70] R. Santos, S. Gorb, V. Jamar, and P. Flammang. Adhesion of echinoderm tube feet to rough surfaces. *Journal of Experimental Biology*, 208(13):2555, 2005.

[71] Scuba.com. Sherwood 80 Cubic Foot Aluminum Tank. `http://www.scuba.com/scuba-gear-200/043077-042005/Sherwood-80-Cubic-Foot-Aluminum-Tank.html`, 2009.

[72] SeacomLive. How undersea cables are laid. `http://www.youtube.com/watch?v=XQVzU_YQ3IQ`, May 2010.

[73] K.P. Sebens. Population dynamics and habitat suitability of the intertidal sea anemones Anthopleura elegantissima and A. xanthogrammica. *Ecological Monographs*, 53(4):405–433, 1983.

[74] P.K.S. Shin, A.W.M. Ng, and R.Y.H. Cheung. Burrowing responses of the short-neck clam Ruditapes philippinarum to sediment contaminants. *Marine pollution bulletin*, 45(1-12):133–139, 2002.

[75] A.H. Slocum. *Precision machine design*. Society of Manufacturing, 1992.

[76] B. Springer. Holding Power. *Sail Magazine*, October 2006.

[77] S.M. Stanley. Bivalve mollusk burrowing aided by discordant shell ornamentation. *Science*, 166:634–635, 1969.

[78] S.M. Stanley. Functional morphology and evolution of byssally attached bivalve mollusks. *Journal of Paleontology*, 46(2):165–212, 1972.

[79] S.M. Stanley. Why clams have the shape they have: an experimental analysis of burrowing. *Paleobiology*, 1(1):48–58, 1975.

[80] T. Stephens. How a swiss invention hooked the world. *swissinfo.ch*, `http://www.swissinfo.ch/eng/Home/Archive/How_a_Swiss_invention_hooked_the_world.html?cid=5653568`, 2007.

[81] STUDIOLEX, Visser & Smit Hanab UK Ltd. Underwater cable laying. `http://www.youtube.com/watch?v=d9tRmJLOCdg`, June 2010.

[82] J.K. Sveen. An introduction to MatPIV v. 1.6.1. `http://folk.uio.no/jks/matpiv/`, 2004.

[83] H. Tennekes and H. Tennekes. *The simple science of flight*. MIT Press, 1996.

[84] K. Terzaghi, R.B. Peck, and G. Mesri. *Soil mechanics in engineering practice*. Wiley-Interscience, 1996.

[85] S.P. Timoshenko and J.N. Goodier. *Theory of elasticity*. McGraw, New York, 1970.

[86] E.R. Trueman. Observations on certain mechanical properties of the ligament of Pecten. *Journal of Experimental Biology*, 30(4):453, 1953.

[87] E.R. Trueman. Bivalve mollusks: fluid dynamics of burrowing. *Science*, 152:523–525, 1966.

[88] E.R. Trueman. Observations on the burrowing of Arenicola marina (L.). *Journal of Experimental Biology*, 44(1):93, 1966.

[89] E.R. Trueman. The Fluid Dynamics of the Bivalve Molluscs, Mya and Margaritifera. *Journal of Experimental Biology*, 45:396–382, 1966.

[90] E.R. Trueman. The dynamics of burrowing in Ensis (Bivalvia). *Proceedings of the Royal Society of London. Series B. Biological Sciences*, 166(1005):459, 1967.

[91] E.R. Trueman. Burrowing habit and the early evolution of body cavities. *Nature*, 1968.

[92] E.R. Trueman. The mechanism of burrowing of some naticid gastropods in comparison with that of other molluscs. *Journal of Experimental Biology*, 48(3):663, 1968.

[93] E.R. Trueman. The mechanism of burrowing of the mole crab, Emerita. *Journal of Experimental Biology*, 53(3):701, 1970.

[94] E.R. Trueman. *The locomotion of soft-bodied animals.* Elsevier Science & Technology, 1975.

[95] E.R. Trueman, A.R. Brand, and P. Davis. The dynamics of burrowing of some common littoral bivalves. *Journal of Experimental Biology*, 44(3):469, 1966.

[96] S. Vogel and K.K. Davis. *Cats' paws and catapults: mechanical worlds of nature and people.* WW Norton & Company, 2000.

[97] H.R. Wallace. The dynamics of nematode movement. *Annual Review of Phytopathology*, 6(1):91–114, 1968.

[98] C.Y. Wen and Y.H. Yu. Mechanics of fluidization. In *Chem. Eng. Prog. Symp. Ser*, volume 62, pages 100–111, 1966.

[99] S.L. Williams. Experimental studies of Caribbean seagrass bed development. *Ecological Monographs*, 60(4):449–469, 1990.

[100] S.L. Williams. Surfgrass (Phyllospadix torreyi) reproduction: reproductive phenology, resource allocation, and male rarity. *Ecology*, 76(6):1953–1970, 1995.

[101] A.G. Winter, V, A.E. Hosoi, and A.H. Slocum. Method and Apparatus for Penetrating Particulate Substrates. US patent application no. 12455392, June 2009.

[102] D.M. Wood. *Soil behaviour and critical state soil mechanics.* Cambridge Univ Pr, 1990.

[103] J. Zeil and J.M. Hemmi. The visual ecology of fiddler crabs. *Journal of Comparative Physiology A: Neuroethology, Sensory, Neural, and Behavioral Physiology*, 192(1):1–25, 2006.